Technical Design Report for the Upgrade of the ICD for DØ Run II

L. Sawyer
Louisiana Tech University

K. De, P. Draper, E. Gallas, J. Li,
M. Sosebee, R.W. Stephens, A. White
University of Texas at Arlington

DØ note 2686

June 30, 1997

Abstract

The Inter Cryostat Detector (ICD) used in Run I of the DØ Experiment will be inoperable in the central, high magnetic field planned for Run II. In Run I, the ICD enhanced the hermeticity and uniformity of the DØ calorimeter system, improving both missing transverse energy and jet energy resolution. The goals for the Run II ICD are the same.

In this document, the physics arguments for maintaining the ICD are presented, followed by a detailed description of the planned design changes, prototype tests, construction, installation, and commissioning of the device for the Run II DØ detector. Estimates of costs and schedule can be found on //D0SERVER2/Operations/Upgrade Project/ subareas available via DZERO's WinFrame Program Manager.

This detector is not intended to provide any "L0" capabilities (for luminosity monitoring), or to provide any EM coverage in the intermediate region, or to provide additional coverage in the intermediate regions, unlike previous upgrades proposed in this detector region. The ICD upgrade described here maintains most of the Run I capabilities in a high magnetic field environment.

Contents

Chapter 1

An Inter Cryostat Detector for DØ

1.1 Introduction and Motivation

The Inter Cryostat Detector (ICD) plays an important role in DØ calorimetry, both in terms of measuring the energy of jets as well as in the calculation of missing transverse energy ($\not\!\!E_T$). The combination of a rapidly changing material profile and extra uninstrumented material in the intermediate regions of the calorimeters leads to reduced sampling of showers, and hence a degradation of energy measurements for this region. The ICD restores energy resolution by providing additional sampling in this region.

The upgraded DØ detector proposed for operation in Run II includes a 2 Tesla magnetic field in the central detector region produced by a superconducting solenoid extending to $|\eta| < 1.6$. The Run I configuration of the ICD, located just outside the ends of the solenoid, will not operate in this environment because the phototubes cannot be fully shielded from the expected Run II magnetic field of over a kiloGauss in this region. In January 1995, the ICD upgrade review committee recommended the replacement of the ICD for Run II based on the presentations summarized in DØ notes 2281, 2494 and 2519 DØ [4, 3, 5]. In summary, the coverage provided by the inner etas ($1.1 < |\eta| < 1.4$) plays a crucial role in jet energy and missing transverse energy resolution. It is this portion of the ICD that must be replaced.

It is therefore necessary to redesign and construct a Run II ICD that will perform as well as the Run I ICD in this high magnetic field environment. Figure 1.1 shows the location and coverage of the ICD in the Run II DØ detector. The position of the ICD is indicated by the thin rectangular box between the central and end cryostats.

The primary goal in upgrading the ICD will be to move the PMTs to a region of reduced magnetic field. The scintillator tiles and all the electronics will also be rebuilt. In the interest of saving money in the research and development necessary for the Run II ICD, the experience with the Run I ICD will be fully exploited, including the salvaging of as much equipment as possible from the Run I detector. However, because of changes in the fiber and electronic readout system, much R&D is necessary to bring this new detector to fruition.

The following section describes the Run I design and performance. The section that follows gives an overview of the Run II design, described more fully in the chapters to follow.

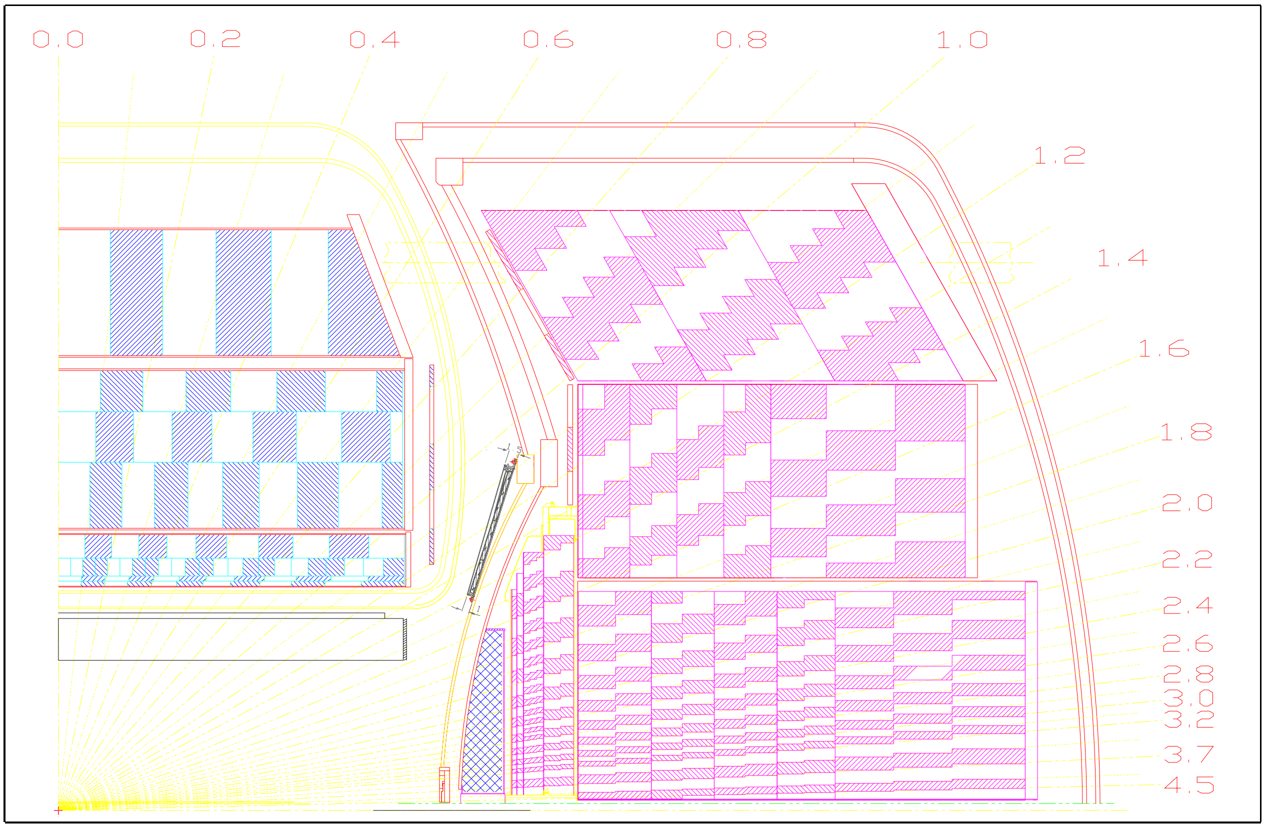

Figure 1.1: Location of the ICD in the Run II DØ detector, indicating the coverage in eta from 1.1 to 1.4.

1.2 Run I Design

The configuration of the ICD during Run I of the DØ experiment was a single layer array of scintillator (Bicron BC-414) tiles, of thickness 1 cm, mounted on the inner face of each end calorimeter cryostat. It was designed to sample the energy of showers which might otherwise be lost in the cryostat walls and spanned the range in pseudorapidity $0.8 \leq |\eta| \leq 1.4$. An ICD "box" consisted of three tiles, each with dimensions 0.1×0.1 in η and ϕ, along with three photomultiplier tubes (PMTs) and associated electronics for the readout of the light signals from the scintillator. Figure 1.2 shows the various components of an ICD Run I box.

The PMTs in all "inner" boxes ($1.1 \leq |\eta| \leq 1.4$) and approximately one-quarter of the "outer" boxes ($0.8 \leq |\eta| \leq 1.1$) were Hamamatsu R647s; the remainder of the outer boxes were equipped with Russian-manufactured PM60s. Light was transported to the PMTs via wavelength-shifting fibers. The preamps through which the PMT pulses are read out were of the same FET hybrid design as those used for the liquid argon calorimeter [1]. A value of 22 pF was chosen for the feedback capacitance in the charge integrating ICD preamps (compared to 5 and 10 pF for the rest of the calorimeter) to lower the gain of the output signals and thereby preserve their dynamic range.

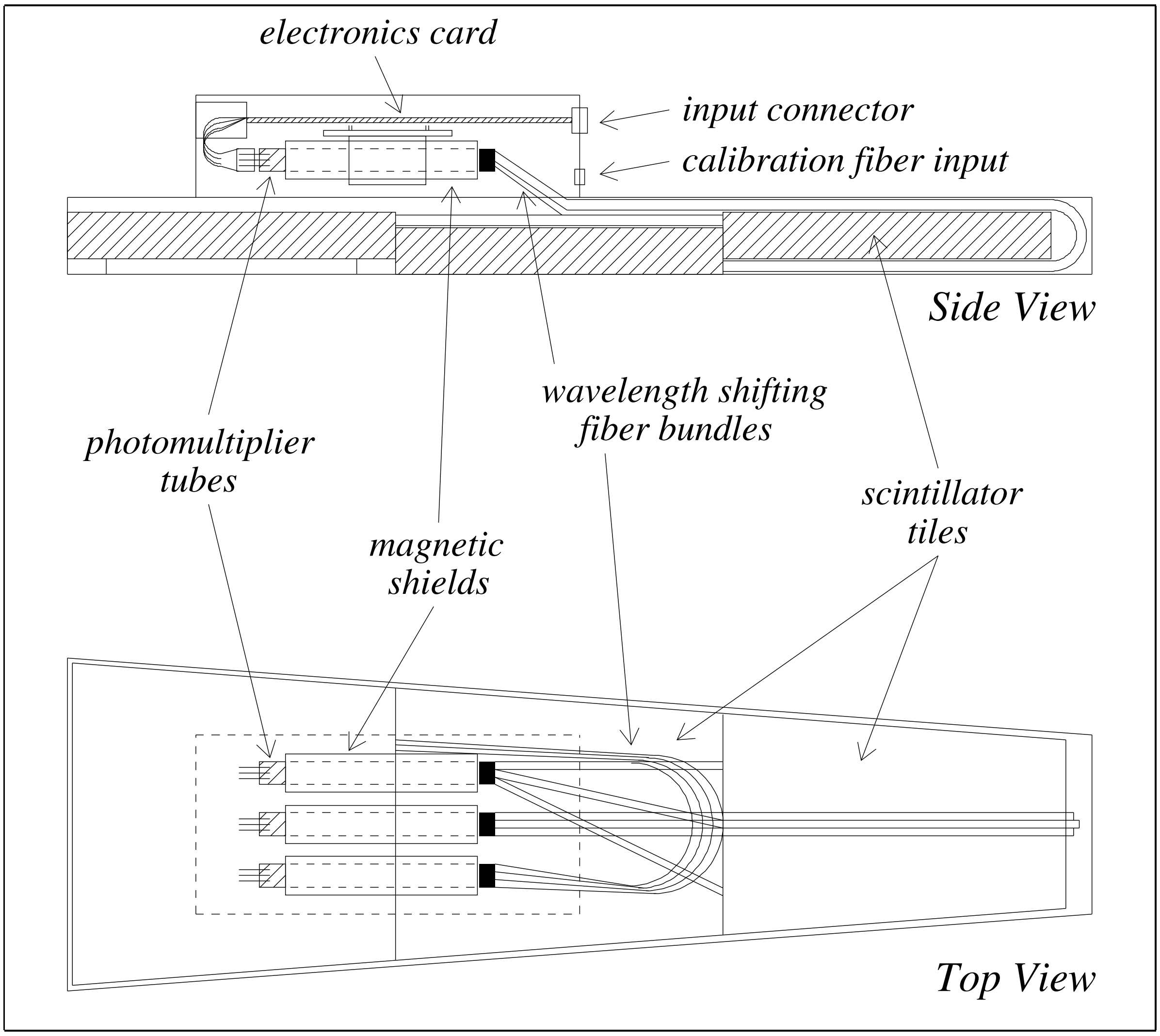

Figure 1.2: Top and side views of an ICD box in Run I, indicating the layout of the scintillator tiles, PMTs, and electronics.

1.2.1 Test Beam Studies

The impact of the ICD on energy measurement and resolution was first demonstrated in calorimeter test beam studies. A mockup of the ICD consisting of 30 tiles with full coverage in η and five segmentations in ϕ, PMTs, and readout electronics was included in the 1991 DØ test beam run [2]. Figure 1.3 shows results for 100 GeV pions, incident upon a region of the calorimeter with ICD coverage, in this case at $\eta = 1.25$ and 1.35. Plotted is the reconstructed energy for some 3000 events, with and without the contribution from the ICD. There is a pronounced improvement in both the central value and the resolution upon its inclusion.

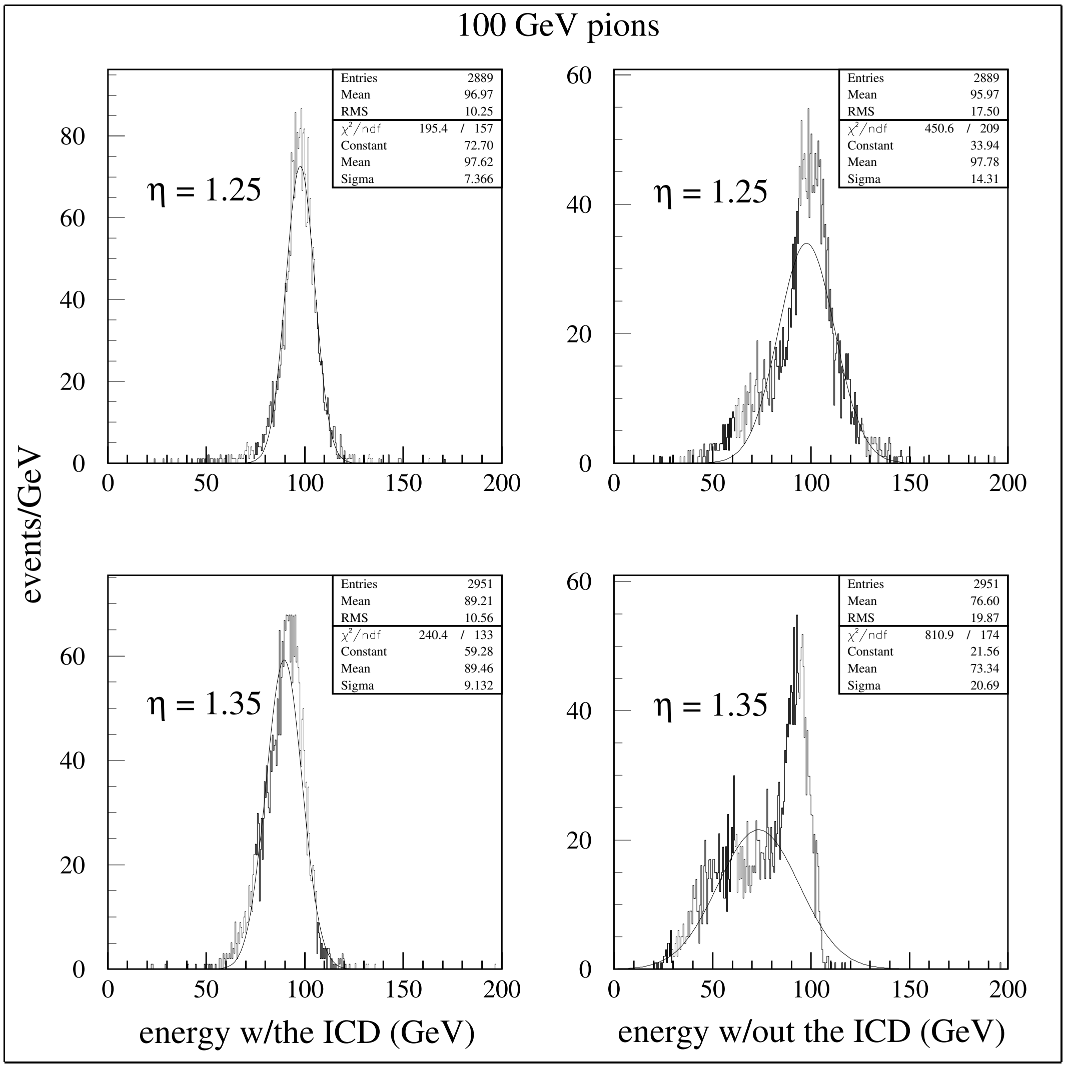

Figure 1.3: Test beam calorimeter response to 100 GeV pions, (left) with and (right) without the ICD.

1.2.2 The ICD in Collider Data

The impact of the ICD on the energy resolution of the calorimeter in the intermediate region has been studied with collider data. The next two sections will describe results from analyses carried out to estimate the contribution of the ICD to jet energy measurements [3] and to the calculation of $\not{E}_T$[4], respectively. In each case results are also shown for the situation where the ICD sampling weights were set to zero to suppress its energy, while the sampling weights for the massless gaps (*i.e.*, the layers of the calorimeter adjacent to the ICD) were reoptimized in an attempt to recover the missing ICD energy. The results lead to the conclusion that the ICD is essential for preserving hermetic and uniform calorimeter performance.

Jet Energy Resolution in the ICD Region

Events with two jets, one (the trigger object) in the central calorimeter, the other confined to the ICD region, were selected for use as a data sample. The central jet was additionally required to have a transverse energy in the narrow range $54 < E_T < 62$ GeV, with the second jet in the ICD balancing against it. In Figure 1.4 is plotted the E_T of the ICD jet for the two cases with and without the ICD energy, at $\eta = 1.25$ and 1.35, as shown earlier for the test beam data.

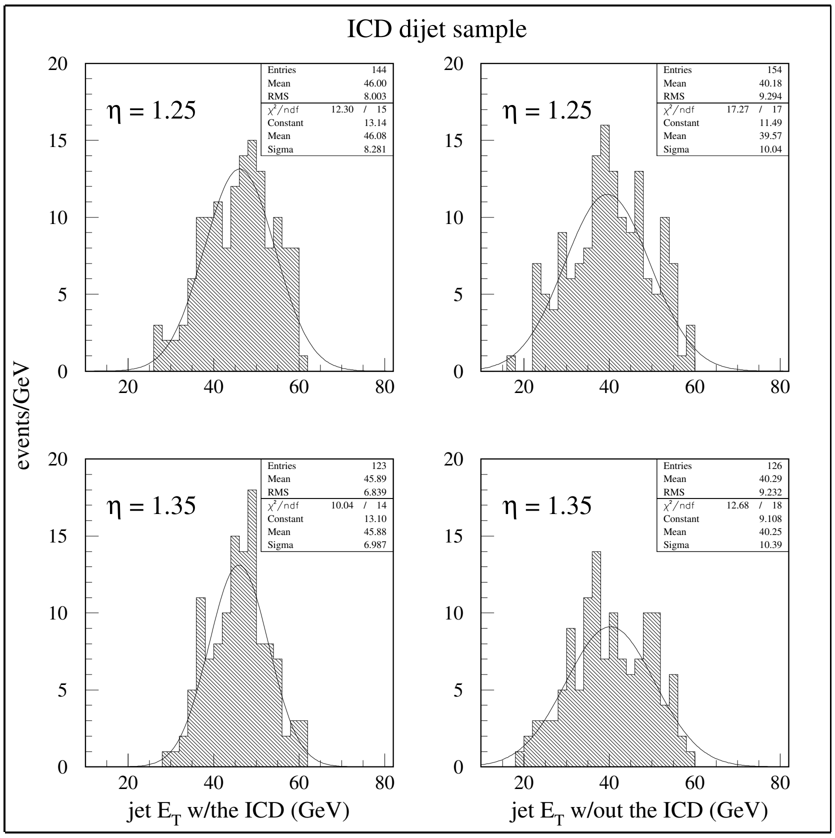

Figure 1.4: E_T of the jet confined to the ICD region, (left) with and (right) without the ICD energy.

Two features reminiscent of the test beam data are notable: (i) the distributions are more broad (*i.e.*, the resolution is degraded) with the removal of the ICD, and (ii) the central values of the distributions indicate that the energy normally sampled by the ICD cannot be fully recovered, despite using reoptimized sampling weights for the massless gaps. Energy resolution is not affected as dramatically as in the case of the test beam data, due to the fact that jets are broad objects distributed over many calorimeter cells in the transverse direction, compared to pions in the test beam studies which deposit their energy in a smaller volume localized with respect to the direction of the beam. Table 1.2.2 summarizes the change in the jet energy resolution (defined here as $\sigma_{E_T}/\sqrt{E_T}$) from the collider data study; test beam results are included as well for comparison.

TABLE 1.2.2

JET ENERGY RESOLUTION VARIATION
WITH THE ADDITION OF THE ICD

Eta Bin	with ICD	without ICD	Δ%	Δ% (TB data)
0.85	108.8%	115.5%	+6.7	+11.8
0.95	94.4%	103.9%	+9.5	+19.6
1.05	113.5%	120.0%	+6.5	+9.7
1.15	109.7%	123.9%	+14.2	+21.1
1.25	118.9%	144.0%	+25.1	+74.3
1.35	101.5%	146.0%	+44.5	+115.2

Impact on Missing E_T

To study the effect of the ICD on the measurement of missing E_T, its energy was removed and the missing E_T recalculated, in an analogous procedure to that used for the jet energy resolution study. Hence, the sampling weights for the massless gaps had again been adjusted to best compensate for the absence of the ICD. The $\not\!\!E_T$ for various data samples were then compared for the two configurations with and without inclusion of the ICD energy.

Figure 1.5 shows the integrated number of events (*i.e.*, the number of events with $\not\!\!E_T$ above a given value) as a function of missing E_T: (a) is for the set of dijet events described in the last section, (b) the same dijet events with the added requirement that the central (trigger) jet satisfy a high-E_T trigger threshold of 85 GeV, while (c) corresponds to a sample of two- and three-jet events which did *not* include a condition that any of the jets necessarily be found in the ICD region of the calorimeter. Because these data samples have little intrinsic $\not\!\!E_T$ associated with them, it is reasonable to assume that whatever $\not\!\!E_T$ they may have is due primarily to detector effects (*i.e.*, finite resolution, incomplete sampling, etc.); thus, we consider this to be "fake" $\not\!\!E_T$.

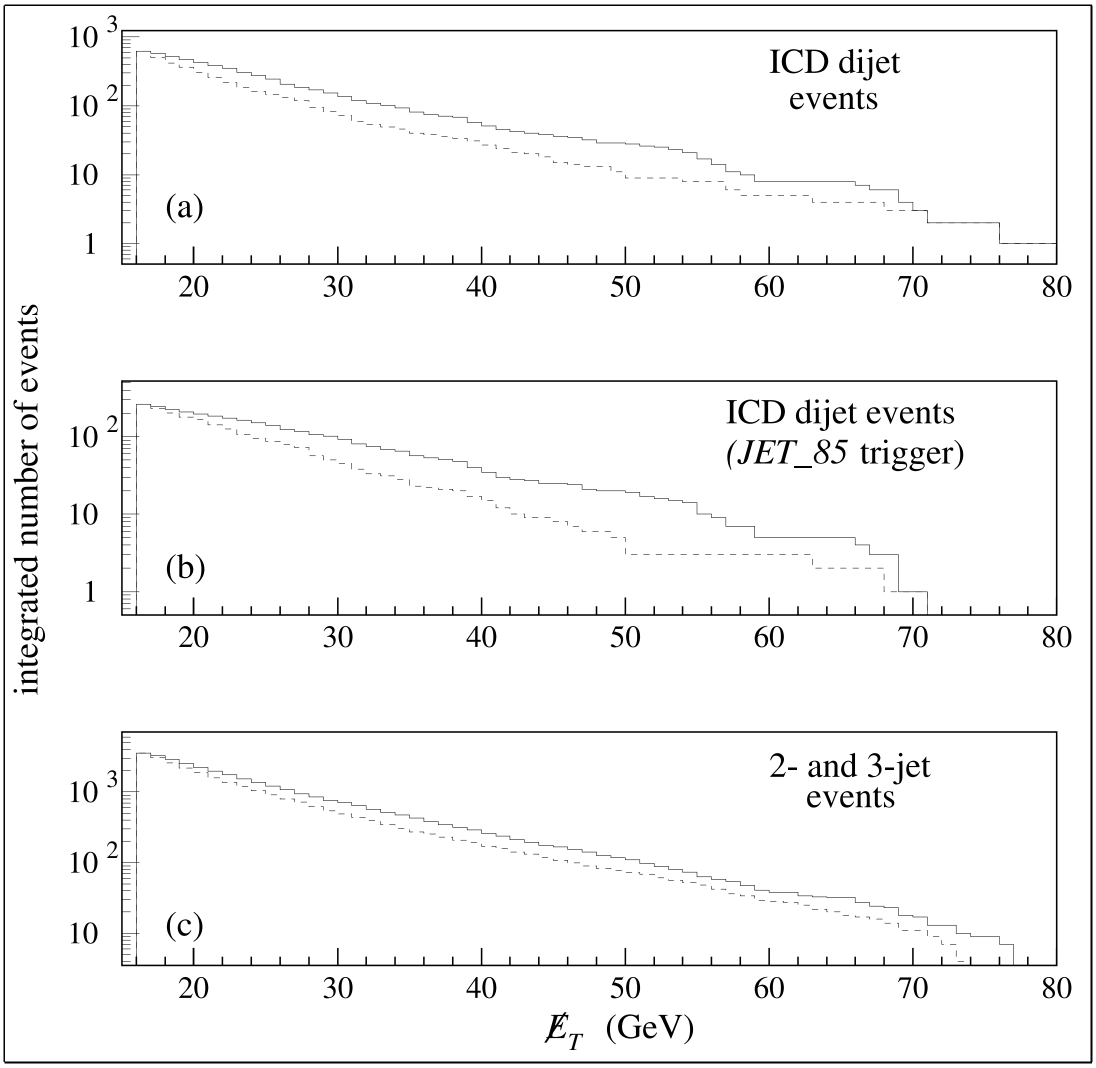

Figure 1.5: Integrated number of events as a function of $\not{E}_T$, with the ICD (dashed lines), and without the ICD (solid lines), for three data sets described in the text.

An increase in the rate of fake $\not{E}_T$ is seen for the data plotted in Figures 1.5 (a) and (b). This was expected, as the requirement that one of the jets be found in the ICD region had been imposed in these events. Note, however, that the rate of fake $\not{E}_T$ is seen to rise in Figure 1.5 (c) as well, despite the fact that no requirement had been made that any of the jets necessarily be in the ICD. This latter result implies that the ICD contribution can be appreciable even in cases where the jets in an event are not specifically confined to those regions of the calorimeter with ICD coverage.

1.3 The ICD for Run II

1.3.1 Performance Requirements

The ICD uses the same digitizing equipment as the DØ liquid argon calorimeters, which places constraints on the ICD electronics design. In combination with the physics performance required, these constraints determine the operating range of the ICD detector for each of the elements - tile system, PMT system and readout electronics.

Tile-Fiber Requirements

We start with the requirements for the tile system. During Run I, calibration with minimum ionizing particles (MIP) played a crucial role in reducing the channel to channel variations which are normal in scintillator based calorimeters. Since there is no calibration system based on radioactive sources for the ICD, the signal from minimum ionizing particles provide the only practical way to calibrate the ICD both before installation and during the run. Therefore, the low end of the operational dynamic range of the ICD should be optimized for a clean minimum ionizing signal.

For Run I, we required a minimum of 10 photoelectrons (pe) from the cathode of the PMT. The statistical distributions of the observed signal in the ICD is determined by the quantum statistics of the photoelectric effect in the cathode. Setting the minimum observable signal to 10 pe provided a signal distribution for MIPs well separated from the pedestal and noise (about 1-2 pe) with a Gaussian width of $\sqrt{10}$ in the peak region. The Landau tails from the noise distribution as well as the signal distribution were well controlled and could be fitted to extract the peak response. Based on our experience with the Run I detector, we therefore propose a minimum requirement of 10 pe for the Run II ICD detector.

Assuming an average quantum efficiency of 10-15% in the Hamamatsu phototubes for the green light emitted by the wave-length shifting fibers, we will need about 80-100 photons from the tile-fiber system. The geometric losses are much harder to calculate in the tile-fiber system, so we cannot specify what thickness the scintillator tile should be. Our experience with prototypes built for the ICD upgrade suggest that a scintillator thickness of 1 cm coupled to two 0.9 mm fibers should provide sufficient light to meet the minimum requirement of 10 pe (i.e. 80-100 photons).

The maximum light output from the tile-fiber system is not important to specify since we do not expect any saturation effects in the scintillator or WLS fiber for our application.

Electronics Requirements

The dynamic range of the ICD electronics must conform to the range of the digitizing electronics. The least count of the ADC is approximately 100 microvolts. The maximum linear output is about 3 volts. The ICD preamplifier is designed to operate linearly within this range.

Monte Carlo and test beam studies for the Run I ICD showed that the maximum signal in a single ICD tile (0.1 in eta and 0.1 in phi) is expected to be the equivalent of 500 MIPs. This number is larger than expected in hadronic calorimeters since DØ does not have electromagnetic sampling in the region covered by the ICD. For example, the ICD layer occurs at electromagnetic shower maximum near $\eta = 1.1$. However, the number of radiation lengths traversed by particles incident on the ICD varies as a function of eta. Therefore, the ICD intercepts particles at different longitudinal shower depths at different etas. A large dynamic range is essential in sampling ICD energy.

Assuming a maximum signal of 500 MIPs, the maximum signal for 1 MIP in the ICD is 6 millivolts. We expect the maximum variation of the channel-to-channel ICD MIP response to be a factor of two higher than the average value. Therefore, we set the average MIP response of the ICD to be 3 mV. The minimum MIP response is then 1.5 mV (factor of two below the average). Since the minimum photoelectron yield is 10 pe, we obtain 1.5 least counts in the ADC (=150 microvolts) for a single photoelectron. Though this number is small, it is well within the capability of the DØ ADC system. Pedestals due to 1 pe noise will then represent a few counts in the ADC system.

During Run I, the ICD preamps used a feedback capacitance of 22 pFarads. This corresponds to 0.033 pCoulombs of charge from the PMT for an average minimum ionizing particle, or about two hundred thousand electrons.

PMT Requirements

We require an average of 10 pe yield at the photocathode of the PMT, and an average 200,000 electrons from the anode. Therefore, the optimal gain for the photomultiplier tubes should be 20,000.

Hamamatsu R647-01 tubes from Run I will be salvaged and reused for Run II. These PMT's have typical rated gains of about one million. This is a factor of 50 more than needed for the ICD! Lowering the operating voltage by the 400-500 volts needed to reduce the gains is outside the operating range of the tubes.

A specially optimized high voltage divider chain (base) was used to achieve such low gains for the ICD, based on an earlier design used by the CLEO experiment. The middle stages of the photomultiplier tube were operated as gain-killer stages with effective unit gains. The high voltage for the remaining stages were tapered due to the linear-focused structure of the dynodes.

The low operating gain of the ICD PMT tubes also helped to extend their longevity. Primarily, PMT aging is a function of the integrated current in the anode. Low gains reduce the total current and therefore extend the useful life of the tube. This is of particular importance for Run II since the ICD tubes are now almost a decade old!

The base design for Run I was also optimized to run at very low currents - about 100 milliamperes. These low currents protect the tubes from being damaged if very large photon pulses are incident on the cathode. When the base current is 100 mAmps, the current at the anode from large signals saturate around 50 mAmps due to space charge effects. Since 50 mAmps is the maximum rated current for the R647-01, we are protected from damage to the anode due to large pulses that may be experienced near the main ring or during Tevatron beam tuning.

During Run I, we experienced a large variation in the operating voltage of the R647 tubes. For some tubes, the operating voltage was too low for efficient electron collection at the anode or the cathode. This problem was worse due to the low gains and currents of the ICD bases. We used diodes operating in zener mode to maintain a constant 125-150 volts at the anode and the cathode.

Finally, in order to maintain linearity over the large dynamic range of the DØ ADC system - 32,000 counts - we adopted a very tapered HV distribution at the stages near the anode and used capacitors to provide extra charge in these later stages.

1.3.2 Summary and Overview

The Run II ICD design includes scintillating tile as the active element (like the current ICD) because of its low cost per unit area, energy resolution, and its ability to operate at room temperature and pressure. Like the Run I ICD, tile segmentation will be 0.1 by 0.1 in η and ϕ. Light signals from the 384 ICD tiles will be transported along clear fibers to the location of the new readout system (about 8 ??? meters from the ICD tile location). The only input/output into the ICD region will be the scintillator output signals. Due to the long fiber lengths involved, tile/fiber material from the Run I ICD cannot be salvaged. We plan to acquire new scintillators and fibers. Chapter 2 describes the current design for the tile modules and the fibers and connectors within them. Appendices A and B describes tools which we have developed for the polishing connectors and splicing fibers in the laboratory at UTA.

A simulation was performed to estimate the cumulative damage to the ICD scintillator in the Run II environment. These results are presented in Section 2.12.

Before installation in the DØ detector, tile modules will be tested offline on a cosmic ray test stand described in Appendix C. This testing will also provide corrections for channel-to-channel variations inherent in tile/fiber calorimetry.

Clear fiber cables, described in Chapter 5, will bring the light signals from each ICD module connector to the readout crate outside of the calorimeter. There is such a crate in each of 4 quadrants, containing phototubes and readout electronics. The crate is mounted such that it moves within each of the four cable winders (just below the “pig troughs”). The readout system will include Hamamatsu phototubes salvaged from the Run I detector. A description of the content of the ICD crate, including the fiber backplane and photodetection through preamplification is in Chapter 3

In the vicinity of the crates, the magnetic field is expected to be significant but less than 300 gauss. Special considerations must be made to insure that the field does not interfere with the successful operation of the detector, as addressed in Chapter 4.

A test beam is not available upon which to base initial ICD calibration as was done in Run I. We propose to begin Run II with Monte Carlo based calibration constants later enhanced with in-situ corrections based on QCD jet data taken early in Run II. In addition, LED and LASER based calibrations systems are proposed, to monitor the time dependence of the response as well as flag the failure of phototubes. Prototype testing will determine which of the 2 options is preferred. These calibration related issues are laid out in Chapter 6 along with issues expected to arise in ICD commissioning.

Chapter 2

Tiles and Fibers

2.1 Overview

The ICD enhances the hadronic calorimeter coverage in the pseudorapidity region from $|\eta| = 1.1$ to 1.4 as shown in Figure 1.1.

Energy flow through the ICD is is detected via the following processes:

- The active elements in the Run II ICD are arrays of scintillating tile to be placed on the inner face of the North and South End Cryostats (EC). Scintillation (light) is produced in the tile from the passage of particles through the tile.
- Wavelength shifting (WLS) fiber is laid in grooves in each tile. This green fiber converts scintillation light in the tile to light in a wavelength region less likely to be absorbed in the subsequent light path.
- The WLS fibers may be spliced to clear fibers shortly (few mm) after exiting the tile if it is found to be a critical factor in reducing light loss. In any case, the fiber path then leads to a fiber connector at the outer radius of the module.
- Clear fiber ribbon cables transport the light from the outer edge of the tile module to the fiber backplane in a crate located just below one of the pig troughs. There are four such crates for the detector, located in the north-east (NE), south-east (SE) northwest (NW) and south-west (SW) quadrants of the detector. Each ICD crate contains a fiber backplane and photodetector electronics (photomultiplier tubes, preamplifiers and associated electronics) for 96 ICD tiles (one quadrant of the detector).

The current chapter outlines the details of the tile array and fibers. The PMT crate will be described in the next chapter.

We exploit extensively the studies performed to develop the CDF End Plug Upgrade detector [6], which uses a similar scintillator tile-fiber based calorimetry for the CDF Run II detector.

2.2 ICD Tile Array

Shown in Figure 2.1 is a schematic of an ICD tile module array, one of which will be placed on the inner face of each of the calorimeter end cryostats. Each array contains a single layer of scintillator tile segmented by 0.1 in η and ϕ. A tile array is ideally composed of 16

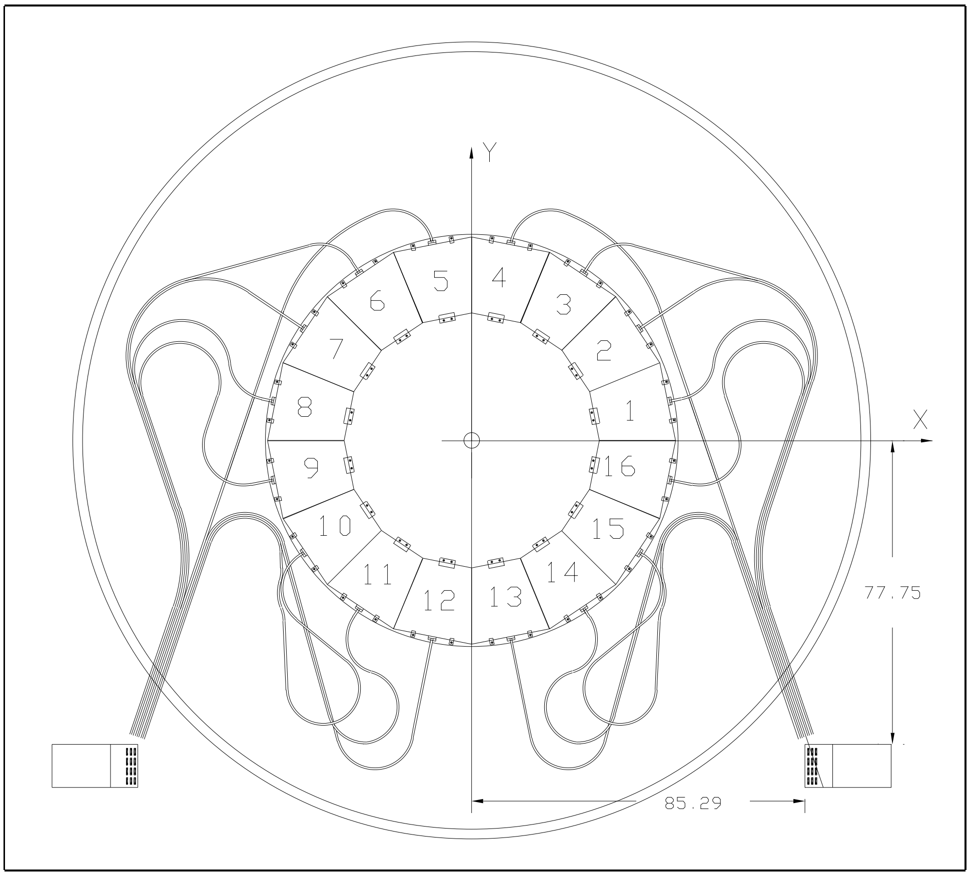

Figure 2.1: Schematic of the ICD tile array to be hung on the inner surface of each of the end cryostats for Run II. The array is composed of 16 identical tile modules.

identical tile modules. If necessary, gaps in complete coverage will be left to allow space along the south end cryostat for the solenoid chimney as described in the next section.

In later sections we describe the motivation for the particular scintillator, fiber and phototubes chosen, details of the module assembly, scintillator routing, cutting and laying of fibers and fiber connectors.

2.3 Gap for Solenoid Chimney

A chimney containing cryogenic, control and monitoring service lines to and from the solenoid magnet will pass between the central cryostat (CC) and south end cryostat. It will take up almost the entire gap in the z direction from the inside radius of the solenoid

(21″) to just past the knuckle on the south EC. It also uses up most of the gap from a radius of about 54″ to the outer radius of the calorimeter.

The chimney path is centered on an angle of $-27.054°$ below the horizontal. The width of the gap needed to clear in phi is 7.25″ [7]. There are 4 ICD tile modules in this quadrant of the calorimeter. Their angular extent relative to the horizontal is indicated in the table here.

Angular extent of 4 ICD modules in a quadrant of the array		
Module number	Angular extent below horizontal	
1	$+0.0°$	$-22.50°$
2	$-22.50°$	$-45.00°$
3	$-45.00°$	$-67.50°$
4	$-67.50°$	$-90.0°$

Table 2.1: Angular extent of modules in the quadrant below the horizontal.

The approximate distance from the beampipe to the inner radius of the ICD tile module is 32″. At this radius, the chimney width (7.25″) occupies a azimuthal angular region of about 13°. The table below shows the angular extent of the chimney at the ICD module inner radius, where the space limitations are most acute.

Angular extent of the solenoid chimney at the ICD inner radius in degrees below horizontal		
chimney	$20.554°$	$-33.554°$

Table 2.2: Angular extent of the solenoid chimney at the ICD inner radius.

At the ICD inner radius, the overlap between the chimney and the ICD array occurs almost entirely within the second module in the table above. On the boundary between modules 2 and 3, there is over 11° (6″) to spare on one edge between the chimney and module 3. On the other side, the chimney cuts into the space of the first module by almost 2° (1.1″).

Using the current design, part or all of module 2 may need to be removed, and additionally part of module 1. Thickness of the tile will be discussed in a later section, which may play a part in how much of the modules need to be eliminated. In addition, consideration must be made to insure that the support rings passing through the region of the missing ICD module likewise do not interfere with the chimney.

Similarly, at the north end of the solenoid, an instrumentation port is expected to occupy the same width in ϕ, and depth in z. The port itself does not extend radially too much further than a radius of 28″ (ICD starts at about 32″). However, some electrical connectors and cables will be attached to this port which will run in line with the $-27.054°$ radial path. It has been suggested that the same "mirror image" gap exist on both the north and south sides.

As more details of chimney and cable routing become available, it may be possible to rework the design to stagger the modules such that a minimum number of channels is lost. A symmetric detector is of the utmost importance for accurate missing transverse energy measurement. In addition, maintaining signals arranged by trigger tower (.2) in η and ϕ, is imperative.

2.4 Choice of Materials - Spectral Matching

Because funding is not available to buy new phototubes, design considerations are driven by the need to reuse the Run I ICD phototubes (1/2″ diameter Hamamatsu R647 PMTs). A major factor in the choice of scintillator and fiber material is the optical matching of scintillator emission, fiber absorption and emission, and optical sensitivity of the PMTs. These spectra are shown in Figure 2.2 [8, 9].

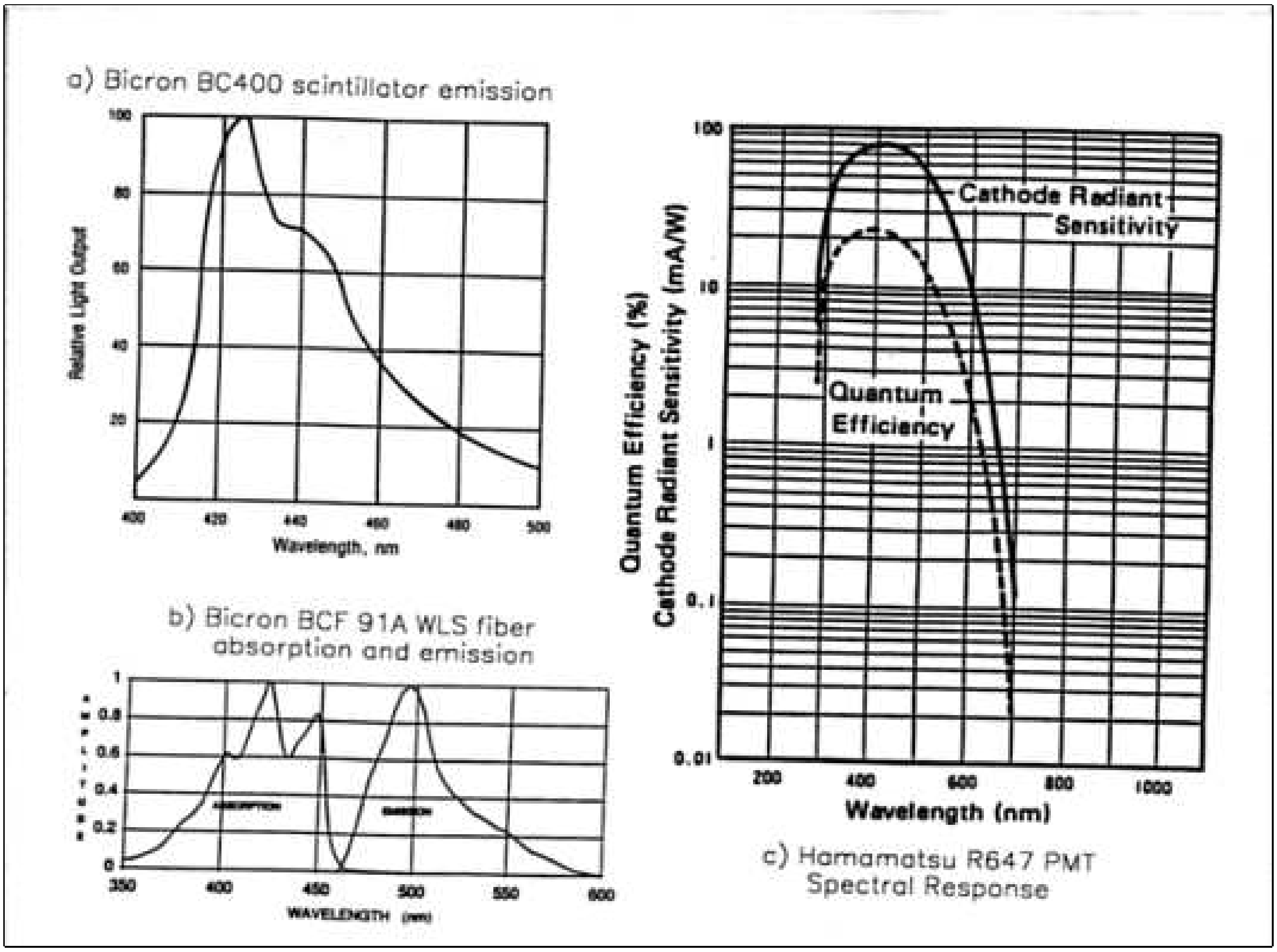

Figure 2.2: Wavelength dependence of the a) Bicron BC 400 emission spectrum, b) Bicron BCF 91A WLS fiber absorption and emission spectra, and c) spectral response and quantum efficiency for Hamamatsu R647 photomultiplier tubes (1/2″ diameter).

The current design includes 1/2" (500 mils or 12.7 mm) thick scintillator of type Bicron BC 400. BC 400 is a general purpose plastic (PVT-polyvinyltoluene) scintillator sensitive to α, β, γ radiation, fast n, as well as charged particles. Unlike inorganic scintillators, it is easily machined. It is radiation hard and stable when exposed to water or isopropyl alcohol typically used for cleaning the scintillator surfaces. It has a relatively high light output relative to other plastic scintillators, with a fast output pulse followed by a moderate decay constant (2.4 ns). Its attenuation length (250 cm) is quite long in comparison to the maximum extent of a single tile (about 20 cm).

Figure 2.2 a) shows the emission spectra of Bicron BC 400 scintillator. The emission spectrum peaks at a wavelength of 423 nm. Emission drops to less than 50% relative to the peak outside of a wavelength range from 415 to 453 nm. This scintillator is well matched to the absorption spectrum of Bicron BCF 91A, as shown in Figure 2.2 b). This multi-peaked spectrum demonstrates highest absorption (above 60% in relative amplitude) in the wavelength range from between 400 to just over 450 nm.

This WLS fiber converts scintillation light in the tile to light in a (green) wavelength region less likely to be absorbed in the subsequent light path. The emission spectrum of this fiber is also shown in Figure 2.2 b). This spectrum peaks at 494 nm, dropping to less than 50% of its maximum amplitude outside of the range from 477 to 517 nm.

This emission spectrum is not ideally matched to the spectral response of Hamamatsu R647 phototubes as shown in Figure 2.2 c). Ideally a blue fiber would be used, but such fibers are no longer available commercially. The cathode radiant sensitivity and quantum efficiency peak at around 420 ± 30 nm. The sensitivity drops to about 60% of its peak value by about 500 nm. While the match is not optimal, the tube sensitivity should be adequate to meet our light collection requirements if the tubes have not degraded significantly D.

2.5 Scintillator Routing

Each tile module contains a sheet of scintillator cut as indicated in Figure 2.3. The piece contains 12 mechanically bonded but optically isolated tiles covering 0.3×0.4 in η and ϕ. The outer edges of the tile form a quadrilateral with 2 parallel sides. Isolation and fiber grooves are cut in 2 stages on the Thermwood routing machine in Lab 8 at Fermilab.

2.5.1 Isolation Grooves

First, isolation grooves are cut, as indicated by the straight lines inside the tile module boundary of Figure 2.3. These grooves are $1/16''$ wide and 490 mils deep, leaving about 10 mils of material for mechanical stability during the epoxying process.

Reflective white epoxy is injected into the isolation grooves using a compressed air dispensing tool [10]. This epoxy serves to optically isolate the individual tiles and to stabilize the individual tiles mechanically into a single rigid sheet.

Formulation and testing of the reflective white epoxy was developed by CDF as described in Reference [11]. Briefly, the epoxy base resin is Dow Corporation DER-332 epoxy. After doping with titanium dioxide powder (commonly used as the primary whitener in commercially available latex paints), it becomes an opaque white reflective epoxy. The epoxy hardens forming a cohesive mechanical bond with unpolished scintillator, but is susceptible to yellowing at the surface under UV light.

In studies by CDF, this yellowing was not found to occur at the epoxy-scintillator interface presumably because the scintillator absorbs the UV, protecting the epoxy. Care should none-the-less be taken to minimize exposure of the tile to UV light.

Bicron reflective white paint is applied to any incompletely filled isolation grooves which occur due to the slight shrinkage of the epoxy that occurs in the curing process. These gaps should not be large enough to degrade the structural integrity of the unit. Black marker will be applied to the scintillator along the back of the isolation grooves, a technique which has been demonstrated by CDF to reduce cross talk between tiles to about 1% [12].

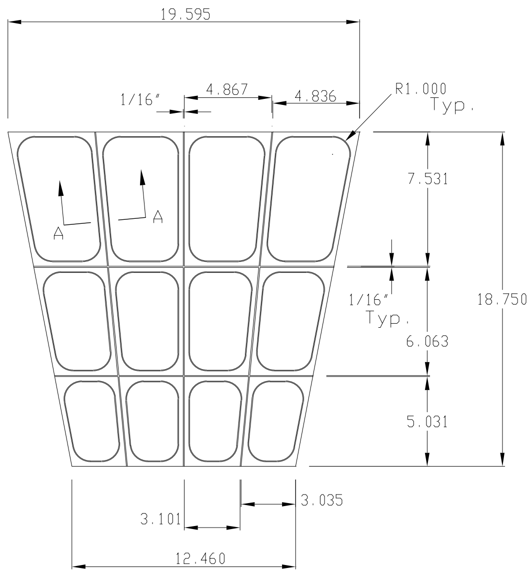

Figure 2.3: Schematic of the scintillator an ICD tile module. Straight lines indicate the isolation grooves. WLS fibers are placed in the curved grooves.

2.5.2 WLS Fiber Grooves

After the isolation grooves have been cut and filled with reflective epoxy, the scintillator is put back on the cutting table to rout the grooves into which the fiber will be laid. The groove location is indicated by the curved loops in Figure 2.3. This contour is motivated by the need to get the groove as close to the tile edge as possible for maximum light collection, and the uniformity, while maintaining a smooth profile to minimize mechanical stress on the fiber as it sits in the groove. Again, results from CDF studies were used to motivate the characteristics of these grooves in the ICD tiles. The final ICD design will depend on results from prototype tiles to be tested later this year.

Figure 2.4 shows a cross section of a tile showing the shape of the isolation and fiber grooves. The keyhole shape of the fiber grooves are created using a ball cutting bit after a rectangular shaped groove is cut. This key, made on the outer edge of the fiber grooves, has been found to be very effective in holding fibers inside the groove without the need for epoxy. Occasionally, quality control will necessitate the removal of fibers from the groove for repair or replacement. The keyhole style groove makes this fiber removal relatively painless.

Light yield uniformity in the vicinity of a WLS fiber groove was found to depend on groove depth. CDF, using scintillator 4 mm (.157″) thick, found that a shallower depth (0.040″) produced a relative 5% increase in light yield [13] in the immediate vicinity of the

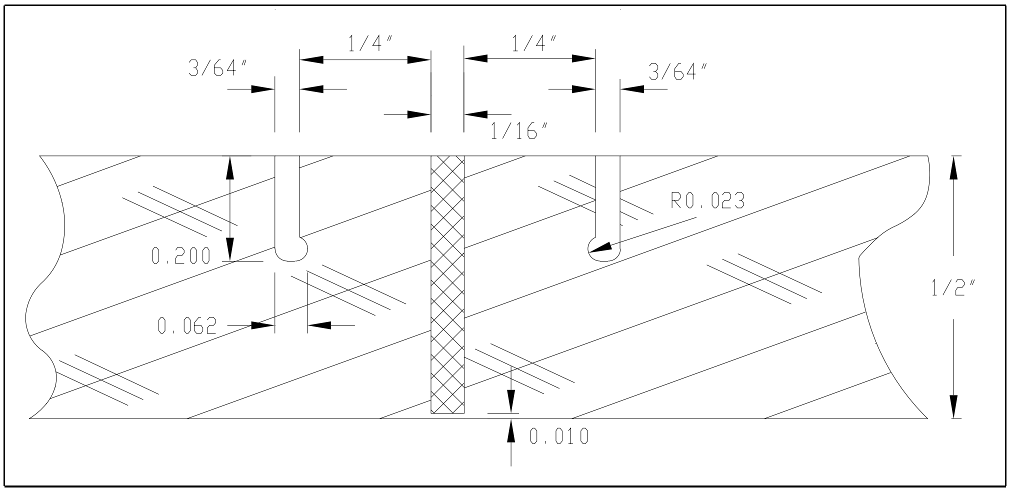

Figure 2.4: Schematic of a cross section of an ICD tile module showing the fiber and isolation grooves. The rounded key in the fiber grooves hold the fiber to out outer edge of the groove, eliminating the need for epoxy.

groove. Presumably, this is due to an increase in light collection efficiency at the groove. A deeper groove (0.100″) produced a corresponding decrease. Ultimately, the CDF design called for a groove depth of 0.065″, which optimized uniformity across the gap with an mean rms variation of less than 2%. As a starting point, DØ prototypes will have a groove depth such that the ratio of groove depth to scintillator thickness is the same as the CDF design. For scintillator .500″ thick, the groove depth will be about .2″. This depth is is large enough to accommodate one or two fibers (of diameter 0.83 mm or 0.033″), two options which will be explored in tile prototype testing described in the next subsection. In the same reference [13], it is noted that little variation in light yield or transverse uniformity was seen as a function of the fiber position within the groove. Therefore, uniformity of response should not depend on where the fiber(s) lie in the groove.

2.6 Fiber Options

The fibers in a tile/fiber calorimeter are well known to be most problematic with regard to quality control and uniform response. If fiber lengths are comparable to or greater than their attenuation lengths, they can also be a significant source of light loss. Wherever possible, double clad fibers will be used; though this is more costly than single clad, the double clad fiber is generally known to reduce light loss. Additional sources of light loss occur where fibers are spliced to one another or connectorized. The ICD group has included many design options in this TDR with regard to fiber configurations. We outline these plans here. Ultimately, the final design depends on prototype tests to be completed in the next year.

2.6.1 Fiber Diameter

The major change in the design of the ICD for Run II is the relocation of the photodetection system to a region just outside the cryostats, where the magnetic field is less intense. Light signals must be transported from the scintillator tile location to the PMT's along along clear fiber ribbon cable. A very limited amount of space is available between the cryostats, so a minimized number of individual fibers is desirable. Therefore, our design criteria includes only one or two fibers per channel between the tile modules and the PMT crate location.

If a fiber is stressed mechanically, crazing or kinking of the fiber results in reduced light transmission or catastrophic failure to transmit light at all. The larger diameter fiber is known to collect more light, but is increasingly more inflexible (and susceptible to damage) as the size increases. Therefore some compromise must be arrived at. We know that beyond a diameter of 1 mm or so, fibers become somewhat inflexible and the fiber in the tile modules and in the ribbon needs to be most flexible. Additionally, it has been suggested that light loss due to mechanical misalignment of fibers at connectors can be eliminated by staging the fiber size smallest to biggest along the light path [14].

We have decided to adopt this staging of fiber diameters along the light path. The fiber diameters we propose for each fiber subsystem are shown in the following table.

Fiber Location	Fiber Diameter
inside tile modules	0.90 mm
fiber cables	1.00 mm
fiber backplane	1.10 mm

Table 2.3: The diameter of the fiber used becomes larger in each fiber subsystem along the light path to reduce light lost due to misalignment of connectors.

Fibers in the tile modules will have a diameter of 0.90 mm, increasing to a 1.00 mm fiber in the fiber cables. The fibers in the fiber backplane will be another 10% larger if the mapping of fibers here will allow it, as described later in this document. Fibers will be potted into connectors with clear epoxy and then the connector ends will be polished flat. The connector polishing tool is described in Appendix B. The connector design, described in a later chapter, includes holes which line up center to center at the fiber-fiber interface. This centering reduces light lost due to misalignment of the fibers since the smaller fiber cross section will generally lie within that of the larger fiber at the interface.

2.6.2 Fiber Layout Options

Three different fiber layout configurations are currently under consideration designated "1α", "1σ", and "2σ". Studies from CDF are available comparing these options, but because we use a different type of scintillator and fiber with different thickness and diameter, respectively, additional prototype testing will be necessary to optimize the current device. The details, and pros and cons of these layouts are described below.

- $\underline{1\alpha}$ - In the 1α configuration, a single WLS fiber is place in each fiber groove. Both ends of the fiber lead to a connector at the module outer radius. It is so named because the greek letter α has two dangling ends.

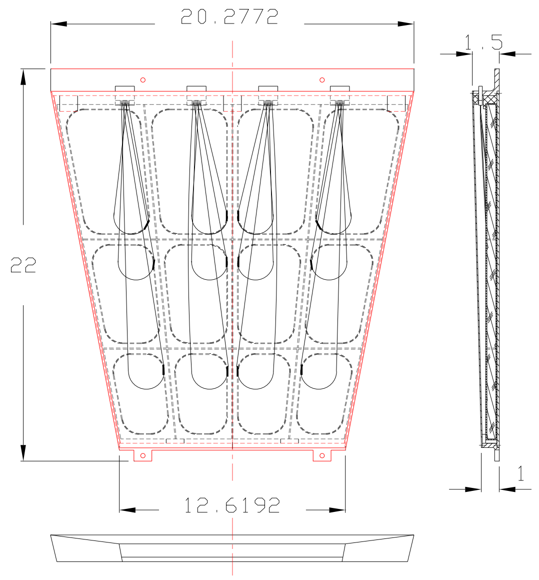

Figure 2.5: Fiber layout in the 1α configuration.

Fiber pathways from the grooves to the connector must be carefully planned to minimize stress that can cause crazing, kinking, or pulling away of the cladding from the fiber core. Figure 2.5 is a schematic demonstrating the path the ends of the fibers might take exiting the tile groove to the connector. In reality, we have found that the 0.9 mm diameter fiber will not easily conform to such tight radial turns, so this option may be eliminated due to production difficulties.

In this configuration, light from a single channel is piped out via two fibers extending from the tile module connector to the fiber backplane (24 fibers per module). This corresponds to 192 fibers per quadrant to be distributed to the 96 PMT's in each crate.

- $\underline{1\sigma}$ - In this configuration, a single WLS fiber is place in each fiber groove. One end the fiber leads to the connector at the module outer radius. It is so named because the greek letter σ roughly corresponds to the shape of the fiber in the groove with one fiber end exiting.

  The other end is "mirrored", ie sputtered with an aluminum coating to enhance reflection at this end. Mirroring of fiber ends can be performed in Lab 7 at Fermilab. Mirroring is reinforced with a drop of glue to prevent it from flaking off while handling or inserting fiber(s) into the groove [15].

  Light from a single channel is piped out via a single fiber to the fiber backplane (12 fibers per module). This corresponds to 96 fibers with a one-to-one correspondence to the 96 PMT's in each crate.

  The major advantage to this layout over the 1α is that fibers exiting the groove can be laid such that their path is nearly a straight shot to the connector. This reduces the path length over which the light must travel, but more importantly, reduces mechanical stress because the fiber does not need to conform to such tight curves. Additionally, production of the "pigtail" (the unit for each tile module containing the fibers potted into the connectors) are simpler to produce and lay in the tile.

  One disadvantage of this layout is that should any point in the fiber path fail, the corresponding channel is disabled.

- $\underline{2\sigma}$ - This configuration is identical to the 1σ layout, with 2 fibers overlaid in the same groove. This layout has all the advantages of the 1σ layout, except that more fibers are involved. Also, if one fiber fails, one fiber remains which may suffice to keep the channel alive.

CDF [16] found that the 2σ layout had higher light yield than both the 1α and 1σ configurations as shown in the table here.

Configuration	# of fibers to PMT	light yield (pe/mip)	yield relative to 1σ
1σ	1(mirrored)	2.3 ± 0.1	1.00
2σ	2(mirrored)	3.4 ± 0.2	1.50
1α	2	3.3 ± 0.2	1.43
2α	4	5.4 ± 0.2	2.35

Table 2.4: CDF measurements directly comparing the absolute light yield of 1σ, 2σ, 1α, and 2α fiber layout configurations. In addition, the 4th column reflects the yield relative to the 1σ configuration.

The 1α layout has a light yield 43% higher than 1σ, but may be too complex from an assembly point of view. While clearly superior from the standpoint of light yield, the 2α configuration is not being considered due to the complexity of assembling this layout (twice as many fibers as 1α).

The 2σ configuration is currently in favor, since it has

1. a light yield 50% greater than that of 1σ and

2. the assembly advantage of reading out only one end of each fiber.

All three options will be tested in a cosmic ray test stand using the same prototype scintillator tiles with grooves as described earlier in this chapter. Factoring into the decision for the final design are light yield and uniformity as well as ease of assembly and quality control.

2.6.3 Splicing Fibers within Modules ?

One source of light loss in a scintillator/fiber detector is the attenuation of light as a function of fiber distance. According to the manufacturer [8], the 1/e decay length of BCF 91A WLS fiber is 3.5 meters. The clear fibers, at a wavelength around 500 nm, have a signal loss of about 0.3 dB/meter which corresponds to an attenuation length of about 9 meters. Clear fiber is used in the fiber ribbon cables (about $16'$ in length) and in the fiber backplane ($< 3'$).

Inside tile modules, WLS fiber is laid in the fiber grooves. It picks up the bluish light from the tiles converting it into the greenish wavelength region less likely to be absorbed in the subsequent light path. The smallest tiles at the module inner radius are furthest from the connector at the module outer radius. The length of fiber from the groove exit point for these tiles to the connector is about 0.6 meters. Because WLS fiber has an attenuation length comparable to this distance, it may be worthwhile to splice WLS fiber to clear fiber immediately after exiting the tile to reduce light loss.

A fiber splicing machine has been built at UTA, based on a design developed by MSU for the CDF collaboration [17]. The fiber splicer is described in Appendix A. Splicing can also be a source of light loss. In addition, it can introduce a change in detector resolution if the quality of splices are not strictly controlled. Therefore, a device for testing the integrity fiber splices is also described in Appendix A.

The testing of prototypes will determine if the there is a non-negligible path length of WLS fiber that causes significant light loss. If so, the fiber splicing option will be explored if this can reduce light loss without causing a significant change in the overall detector resolution. If the splicing option is abandoned, black sleeves may encase the WLS fiber en route to the connector to reduce cross talk between fibers.

2.7 Fiber Connectors

We have explored two options for connectorizing the fiber ribbon cables. Note that a more complete description of the ribbon cables themselves will be given in the "Cabling" chapter. Initial designs included a custom machined connector, and prototypes were made at the UTA machine shop. This option proved to be too expensive. Given the relatively low number of connectors needed, we found it is also uneconomical to pursue having custom connectors injection molded. We then searched for a commercially available alternative.

We have chosen the precision injection molded connectors distributed by DDK Electronics, Inc. A drawing of a connector assembly is shown in Figure 2.6. These connectors

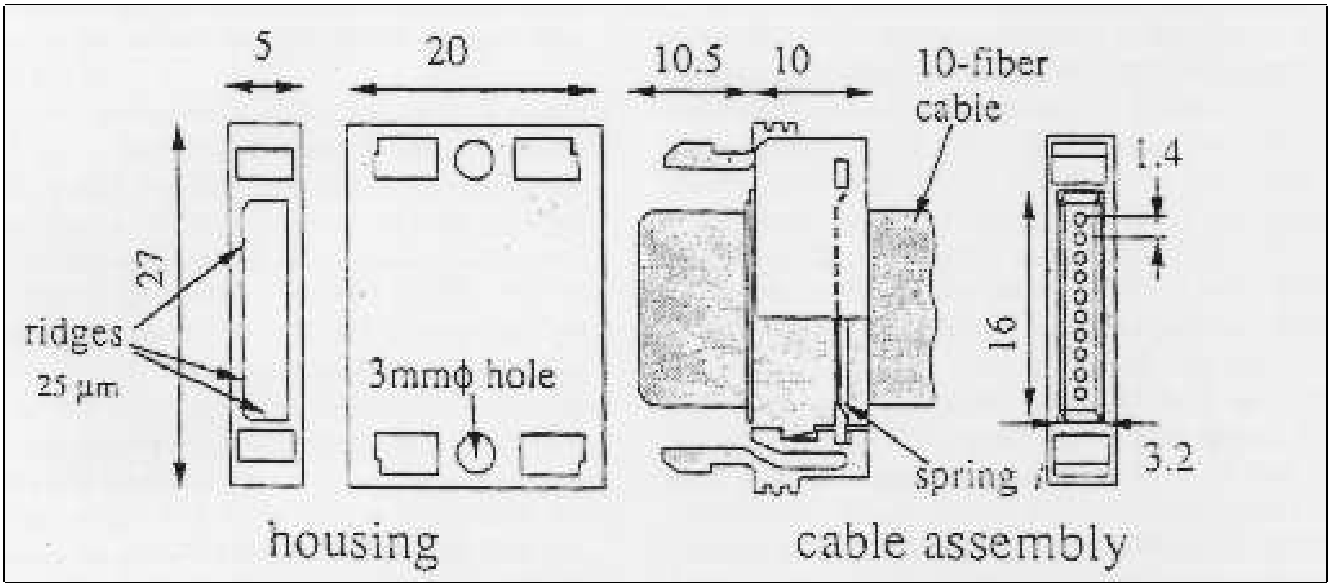

Figure 2.6: Fiber ribbon cable connector.

have been used by CDF and CMS [18]. They are modular and are available in the appropriate sizes for our fiber diameters. This connector is available only in 10-channel models. The most straightforward way to adapt these connectors to our needs is to use three connectors if a 24 fiber/tile fiber configuration is adopted, or use two connectors if a 12 fiber/tile design is decided upon.

2.8 Aluminum Boxes

A light-tight enclosure and mechanical support is necessary to mount the ICD tiles to the face of the EC cryostats. Tile/fiber assemblies will be housed in aluminum boxes which can then be bolted to the cryostat (see next section). Ideally, there will be 16 identical boxes on each EC cryostat as shown in Figure 2.1.

Because precision welded seams on the boxes are cost prohibitive and make disassembly of the boxes for repair difficult, the tile/fiber assembly will be wrapped to make them light tight within the aluminum box. The inside of each box will be painted black.

The boxes have been designed as shown in Figure 2.7 and one prototype has been

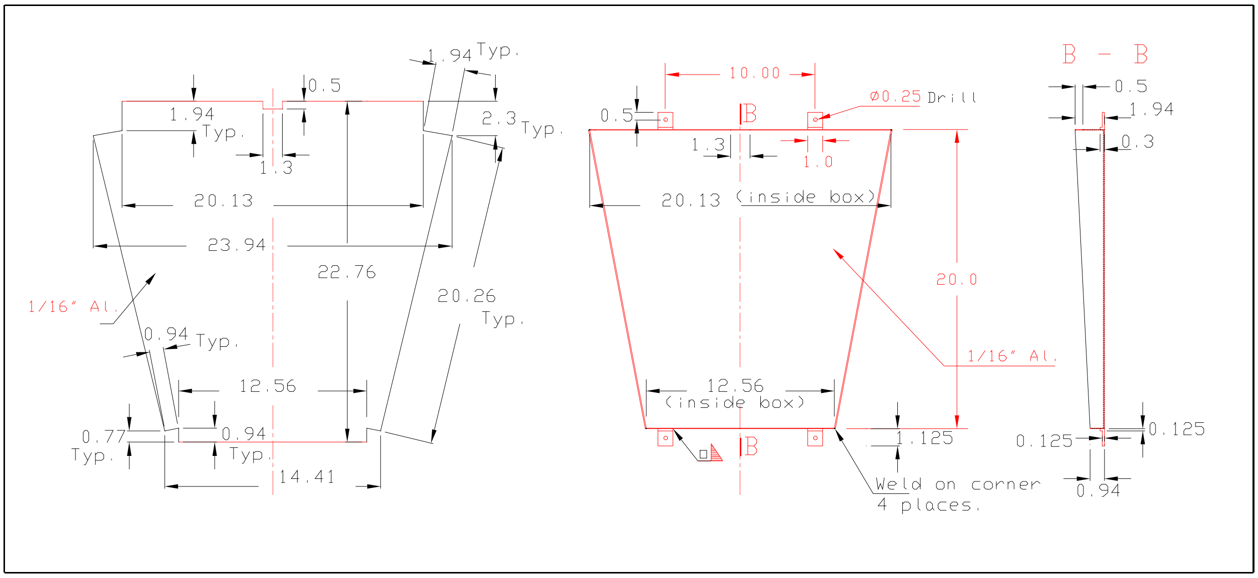

Figure 2.7: Design for the bottom half of an aluminum box designed to house an ICD tile module. The first two pictures show the box design before and after folding. The rightmost picture is the profile view after folding.

fabricated in the UTA workshop. This particular series of diagrams show the design for the bottom of the box with the edges lying flat, with edges folded, and a profile view after folding. Currently one of these prototype boxes is being used to house a prototype tile module at Fermilab for testing.

These boxes will be commercially fabricated to achieve precision folds of the aluminum and a good tight fit between the base of each box and its cover. This is similar to the production of the smaller boxes used for the Run I ICD.

The outer radial edge of each box will contain slots to hold enough fiber connectors to accommodate the number of fibers required from each module. The number of connectors depends on the final fiber layout configuration to be used which will be determined in prototype tests.

2.9 Tile Module Assembly

ICD tile modules are manufactured in the following series of operations:

1. Isolation grooves are cut in a sheet of scintillator and then filled with a white reflective epoxy.
2. Fiber grooves are cut in the scintillator and the tile module is cut out of the sheet.
3. A pig tail, one for each tile module, is made by epoxying the appropriate length of fibers into connectors. The connector end is polished flat.
4. The fibers of a pig tail are inserted into the fiber grooves of the tile module. Connectors lie on the edge of the module with the larger tiles, which will ultimately lie at the ICD array's outer radius.
5. The tile and fibers are wrapped in a layer of reflective white paper called Tyvek [19] then a combination of black felt and a silicone glove to make the tile/fiber assembly light tight.
6. This light tight tile assembly with connectors at one edge is placed in an aluminum box described in the previous subsection.
7. The fully assembled module is tested on the UTA cosmic ray test stand, described in Appendix C, before it is shipped to Fermilab for installation in the detector.

A profile view of an ICD tile module is shown in Figure 2.8. The exterior profile shows the

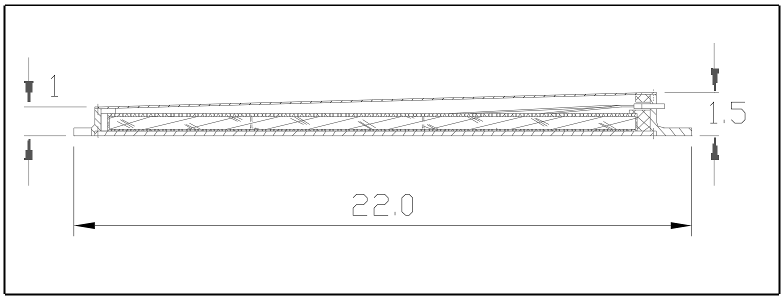

Figure 2.8: Profile view of an ICD tile module. The module is thinnest at the tile array inner radius. It gets thicker at the other end to accommodate wrapping and fibers and connectors.

shape of the aluminum box encasing the scintillator, fibers and wrapping. The interior lines indicate the location of the scintillator within the box.

Space is at a premium in the calorimeter near the central cryostat knuckle (at the ICD tile array inner radius). For this reason, the module is narrowest at this edge, but gets thicker at the other end to accommodate wrapping and fibers as they exit the tile grooves and proceed to the connectors.

2.10 Mechanical Support

In Run I, the ICD tile boxes contained 3 tiles (each covering 3 units in η and one unit in ϕ). Another aluminum box was attached to the top of the tile box which housed the photodetection readout electronics. These Run I boxes were screwed to rails which were attached to welded supports on the face of the end cryostats.

The Run II tile modules now contain 12 tiles (covering 3 units in η, 4 in ϕ), and electronics is relocated outside the cryostat. The heaviest part of the module is the scintillator itself and Run II scintillator is a thicker than that used in Run I. However, the Run II ICD contains half the coverage (half the tiles).

In summary, the weight of the ICD tile modules will not be significantly different than the Run I detector, so we propose to hang it in a similar manner. Aluminum tabs will be provided at the inner and outer radial boundaries of the aluminum boxes to allow attachment to the EC cryostats. Similar tabs, used in the Run I ICD support, were found to occupy very little space in the z direction where space is most critical.

At the inner radius, coordination is necessary with the FPD (Forward Preshower Detector) which may extend to pseudorapidities no less than 1.5. The pseudorapidity region from $1.4 < \eta < 1.5$ is expected to be uninstrumented, so coordinating hardware to mount both detectors in this region is planned.

2.11 Installation

For an extended period during the installation schedule, the south end cryostat is expected to be moved off the platform (onto the sidewalk) to install the Run II central detector subsystems. The bulk of the installation of the Run II central detector subsystems will take place during this time from the south side of the detector. It has therefore been proposed that the north ICD tiles and crates be installed first and the commissioning of the north begin as early in the schedule as possible.

After final testing of tile modules and drawers, installation begins with the mounting of modules on the north end cryostat (described above) and the ICD crates (described in Chapter 3). Protective covers must be installed on all fiber connectors to keep dirt and moisture out during the module and crate installation.

Flexible fiber zipper cables, described in Chapter 5, carry light pulses from the tile modules to the readout crate. For uniformity, all cable lengths will be identical; Their proposed paths are shown in Figure 2.1. Only after crates and tile modules are installed can fiber cabling be installed to minimize agitation or unnecessary bending of the cables.

Because of the limited space available between the cryostats when on the platform, the south ICD tile modules should be installed on the south end cryostat (EC) while it sits on the sidewalk. After the south EC moves back to the platform, installation of the south

ICD PMT crates and subsequent commissioning should then proceed smoothly, having gone through the full process on the north.

2.12 Radiation Effects

The rate of radiation dose and the integrated dose are separate causes of diminished light output in commercial scintillator [31]. Radiation damage in plastic is caused by the formation of light absorbing free radicals in the polymer. Since polymers do not have crystal lattice structure, most of the radicals regroup with polymers resulting in recovery of the light output. However, there is no recovery for dose rates below a critical value of about 4 rad/s for most plastics, regardless of the total dose. Generally, the softer the plastic, the greater the recovery rate. The typical time for maximum recovery is about seven days for most polystyrene (PS) and polyvinyltoluene (PVT) scintillator (ICD scintillator is PVT). A low dose rate which integrates to a large total dose causes the greatest permanent radiation damage [32].

To estimate the total dose and dose rate in the Run II ICD, we assume that the radiation is dominated by minimum bias interactions and are conservative in estimating the other parameters. If we assume:

- three crossings and 99 bunches at $\mathcal{L} = 2 \times 10^{32}$ cm^{-2}sec^{-1} — the important number is the product of average crossings and crossings per second which is larger for 3 and 99 than 6 and 36, thus we make the conservative choice;
- minimum ionizing radiation of 1.8 MeV in a half inch thick piece of scintillator; and,
- 1.7 minimum ionizing particles in a calorimeter tower for each minbias interaction — this is the average number of particles in an ICD cell based on an ISAJET study

then we expect a maximum dose rate of 9 μrad/s. Thus, after a generous three full years of data taking we expect the total dose over the lifetime of the upgraded detector to be less than 260 rad for each ICD tile.

With a dose rate this low we cannot expect noticeable recovery from radiation damage. On the other hand, the total integrated dose is also quite low. Comparing with a measurement in Reference [31], a dose rate of 3.9 rad/s and a total dose of 2.0 Mrad we are very conservative in expecting a decrease in light output of the scintillator due to radiation damage of well under 20%.

We conclude that the Run II ICD performance is not threatened by light losses from radiation damage to the scintillating plastic.

Chapter 3

PMT Crates

The most extensive design and installation project within the Run II ICD will be the construction of the subsystem known as the PMT crates. These so-called crates consist of the following major components :

- The Fiber Backplane This is a closed box on the calorimeter side of the PMT crate. It has connectors on one side to which the fiber ribbon cables will be connected. Within the fiber backplane individual fibers will carry the light to the PMTs. The light signal from the LASER calibration system will also be fanned-out to the PMTs inside the fiber backplane.
- The PMTs Each PMT will be housed inside a mu-metal shield, which in turn will be situated inside a large iron block between the fiber backplane and the drawers.
- The Drawers The readout electronics, PMT bases and electronic calibration will be housed in a series of drawers. There will be six readout channels per drawer and sixteen drawers per crate. The drawers will be designed to be accessible for maintenance and repairs.

A top and front view of the layout of the PMT crates is given in Figure 3.1.

The space reserved for the PMT crates, in the region of the cable winder known as the "pig troughs", is approximately $40''$ width(z) $\times 11''$ height(y) $\times 22''$ depth(x), although this depends somewhat on which side is being considered with more space in z available on the south side of the detector. The overall dimensions of the PMT crate is $30.95'' \times 11'' \times 22''$, which should fit within the allotted space. The dimensions of the iron block is 30.95" x 11" x 3.5" with 96 holes ($15/16''$ diameter) drilled for the PMTs. The room for the fibers within the fiber backplane is $30.7'' \times 11'' \times 6.5''$.

3.1 Fiber Backplane

The function of the fiber backplane is to distribute the light signals from the fiber cables, originating at the ICD tile modules, to the correct photomultipliers located in the crate assembly. The fiber backplane enclosure is located at the rear of the crate assembly (see Figure 3.1). There are four crate/drawer assemblies and fiber backplanes. Each

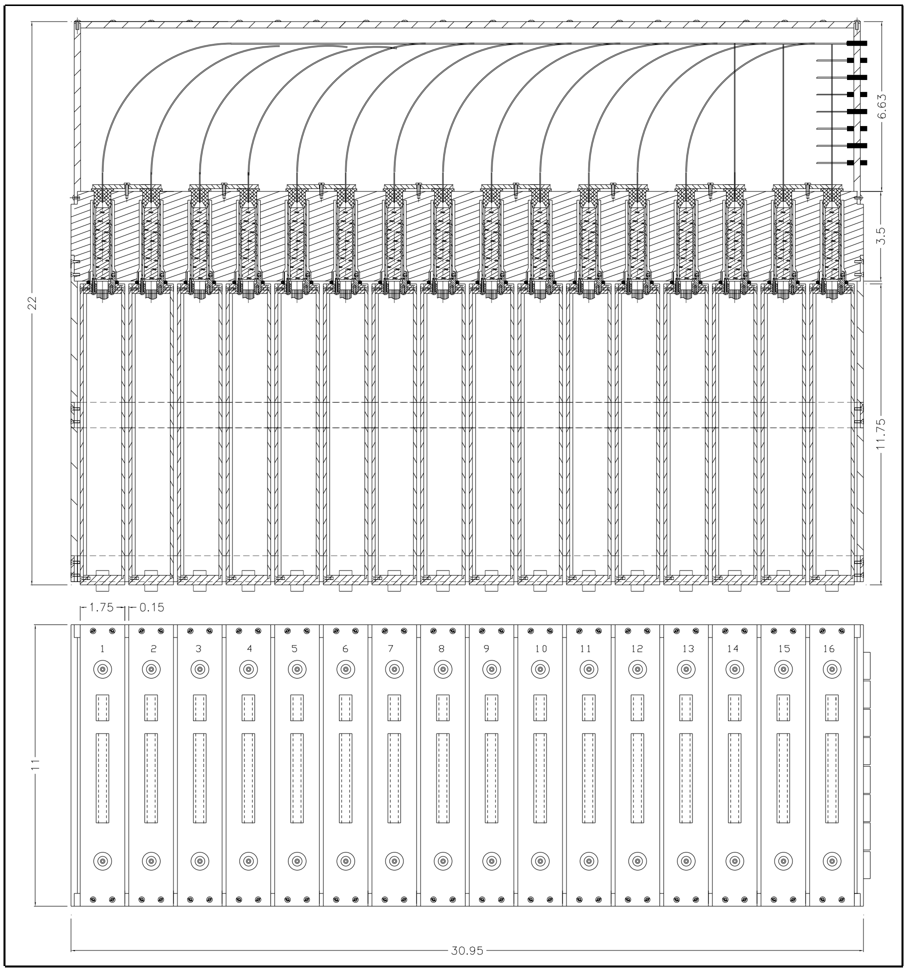

Figure 3.1: Proposed design for the ICD PMT crates. At the top of the figure is a cutaway view of the fiber backplane, PMTs and drawers, looking down on the crate. Below is shown the front view of the PMT crate.

backplane services 96 channels from the fiber cables, mapped on to the array of 16 x 6 photomultipliers. The light pulse from a single tile is carried by two 1.0 mm fibers in the cable. The side of the fiber backplane enclosure carries an array of 32 fiber connectors, arranged as 8 columns of 4 connectors/column. We therefore require 128 connectors for all the fiber backplanes. Each connector carries three pairs of fibers and thus each column of 4 connectors services two columns of 6 photomultipliers. The fibers in the backplane itself will be 1.1 mm diameter to minimize the light loss in the connector. The layout of these connectors is shown in Figure 3.2.

The fiber pairs will be routed within the backplane to the "cookie" which holds the far end of the fibers in the correct location with respect to the photocathode of the photomultiplier tube. Some of the fibers can be routed directly from the connector to the cookie with a simple 90 degree turn. Other fibers, particularly those for which the distance is short, will be looped to avoid a small bending radius. There is a strong requirement for the inside of the backplane to be light tight. Special attention will therefore be paid to

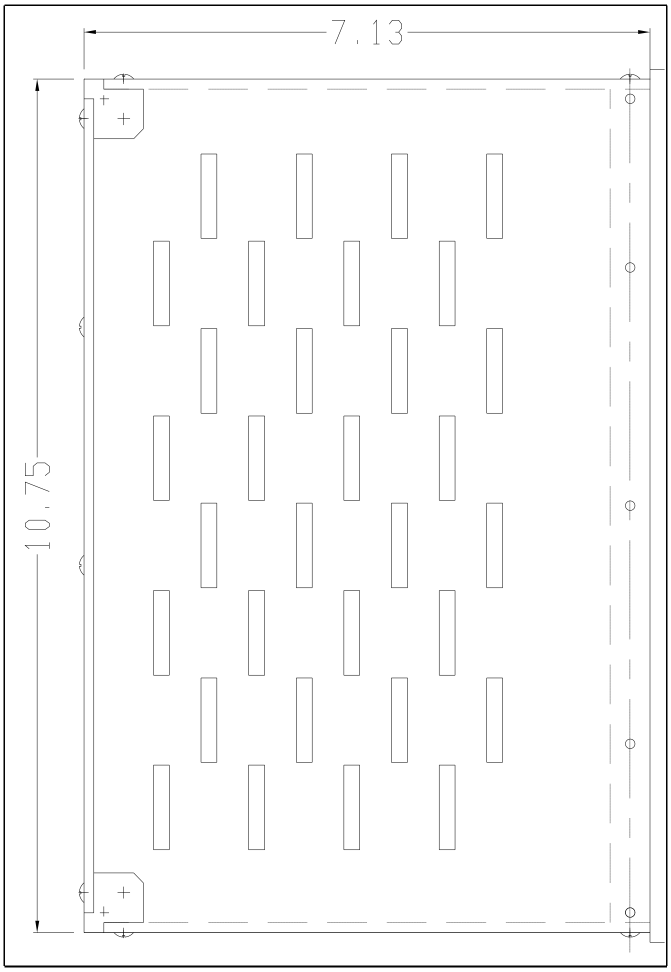

Figure 3.2: Layout of fiber connectors on the side of the fiber backplane.

sealing around the connectors and the seams of the enclosure. Crosstalk between fibers inside the backplane, even if they touch, is expected to be small due to the fibers being clad. A full size prototype fiber backplane enclosure is being developed to determine the optimum fiber arrangement and test assembly procedures.

3.2 PMT Drawer Mechanical Design

The ICD drawers will house PMTs, PMT electronics, and preamplifiers for three or more channels of readout. The number of channels per drawer was determined by both the optimal size of each drawer as well the mapping of drawer to readout channels. Six or twelve is the logical choice since the number of channels in each drawer would form 1 plus one-half of a trigger tower or 2 and two-halves of a trigger tower, respectively. We have chosen six channels per drawer for the final design.

The front of the PMT crate will house a 2-dimensional array of slots holding the ICD drawers. Figure 3.4 shows the proposed design for an ICD electronics drawer. Each drawer will slide individually on Teflon rails, making individual maintenance of each drawer convenient. Internally, the ICD drawers will have fibers entering the PMT housing from the back end through cookies mounted in the fiber backplane. When a drawer is in its slot, six PMTs will be aligned with six fiber bundles from the backplane. The PMTs will be spring-loaded in the custom built mounts attached to the front of the drawer; see Figure 3.3 for a detailed drawing of this mounting fixture.

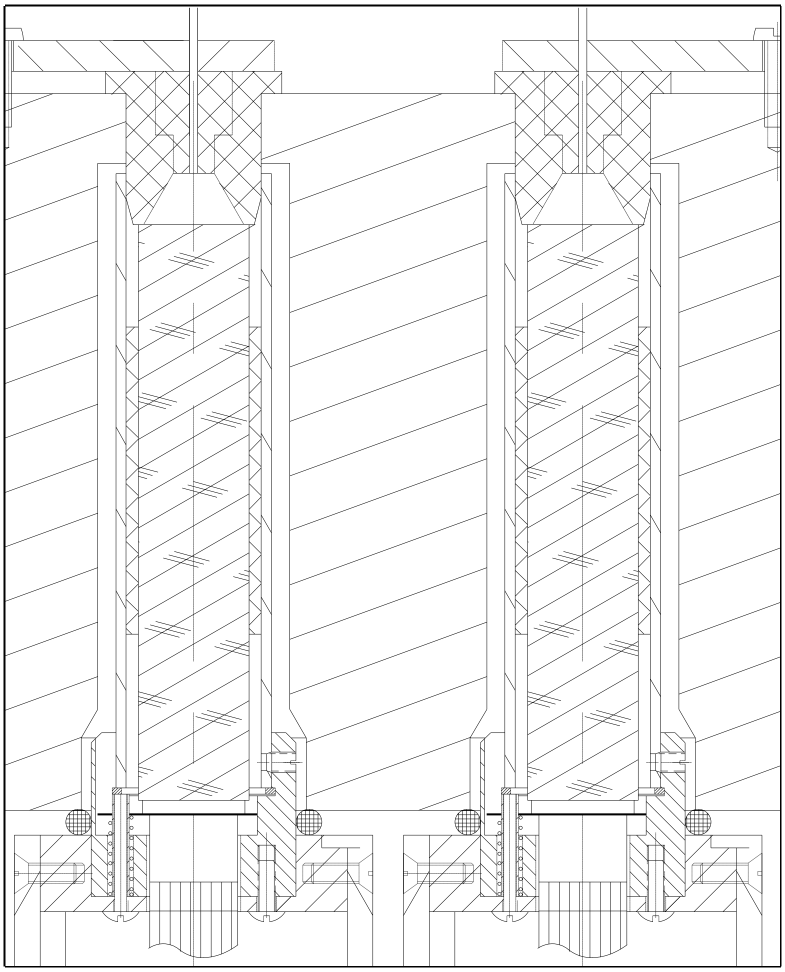

Figure 3.3: The custom designed mounting fixture used to attach the PMTs to the front of the drawers.

The PMT electronics and preamplifier will be located inside the drawer on an electronics card level with the PMTs. Input high voltage and output signal ports will be located on the front of the drawer. A temperature monitoring and heat dissipation system may be required since the power consumption of Run II charge integrating preamplifiers has risen by a factor of ten over the Run I preamplifiers.

Between the fiber backplane and the PMT drawers, there is a large iron block, into which the PMTs (mounted within mu-metal shields on the front of the drawer) will slide. In addition to aligning the PMTs with the cookies containing the signal and laser calibration fibers, this iron block provides the primary shielding of the ICD PMTs from fringe magnetic fields in the region. For a full discussion of the response of the ICD PMTs

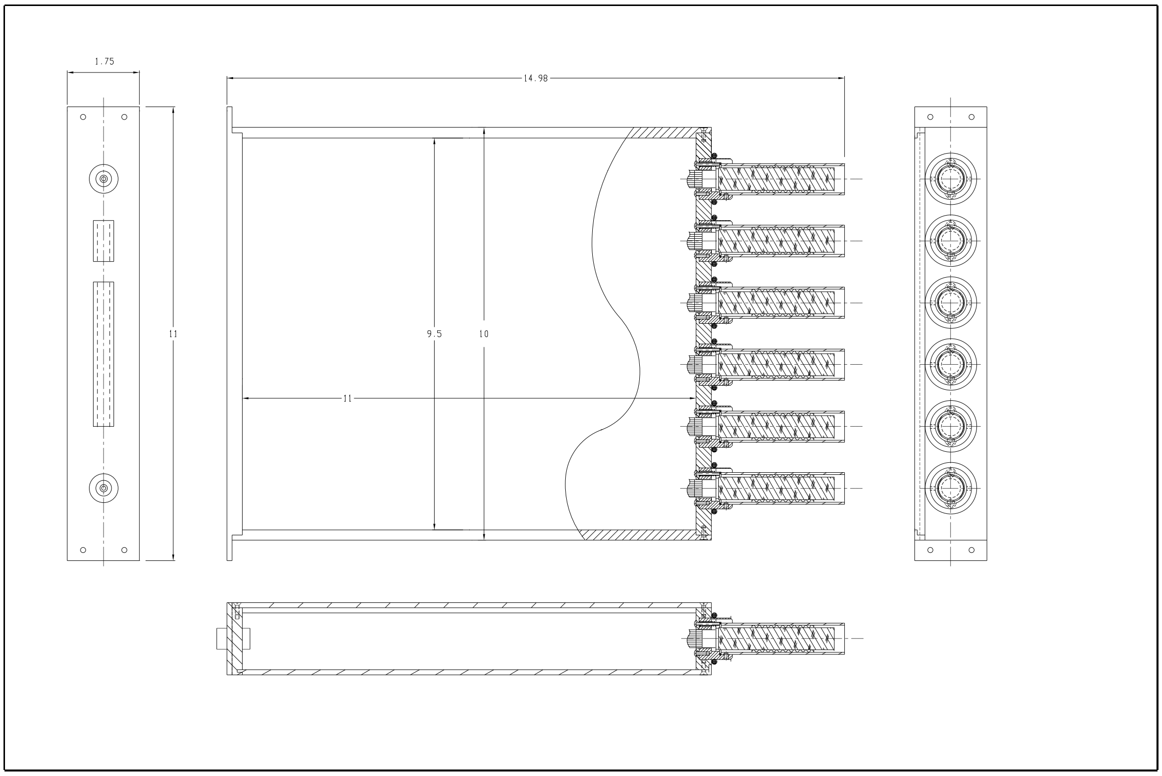

Figure 3.4: Proposed design for the drawers which will house electronics cards and PMTs.

to the expected magnetic field, and studies leading to the current design for the magnetic shielding, see the chapter on magnetic field studies below.

3.3 Electronics

A complete redesign of the readout electronics is necessary in order to be compatible with the DØ BLS system and the DØ Run II preamplifier design. To understand this, a short discussion of the Run I electronics is needed. As has already been mentioned, the Run I ICD box mounted on the ECs housed the electronics board containing three PMT bases and three modified calorimeter preamps. Each box had a high voltage cable coming in to it, and a specialized cable that brought low voltage and calibration signals in to the box and the signal out. Signals were merged together in custom cards, and then sent along a 26-channel twist and flat cable to the BLS cards.

The following modifications have to be made for Run II :

- The custom cables previously used for low voltage and signal were poorly constructed and have already been discarded.
- The preamps for Run II are new and have different low voltage needs. Three voltages are now required : +8 V, -6 V and +12 V.

- There will be six readout channels per board, housed on the motherboard in the ICD drawers.
- The high voltage fanout boxes, previously connected to the ICD boxes, are gone. (The space formerly occupied by these boxes will be used for the ICD PMT crates.)

We therefore will redesign the ICD electronics mother board, incorporating lessons learned in developing the boards for Run I, to be compatible with these changes.

3.3.1 Motherboard layout

For Run II, the ICD electronics motherboard will have a more modular design. Both the PMT bases and and preamps will be on daughter cards mounted to the ICD motherboard. The PMT sockets will connect to a set of solder points at one end of the board. At the other end of the board will be connections for the voltages, pulser signal, and PMT signal out. Other than this, the motherboard will mainly contain traces connecting the base and preamp daughter card sockets.

3.3.2 High Voltage Bases

The HV bases are schematically the same as the bases used for Run I, but made from surface mount components. the layout of this surface mount card is shown in Figure 3.5. The surface mounted daughter card bases will allow easier replacement in case of failure, and lower noise level due the smaller feature size. Currently we have the necessary components, including the blank cards, to produce enough bases for the Run II ICD.

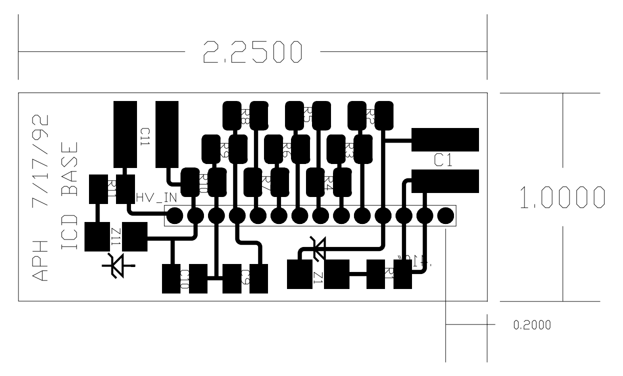

Figure 3.5: Circuit layout of the high voltage base daughter card.

3.3.3 Preamps

The DØ electronics group is aware that the ICD expects to use a version of the Run II calorimeter preamplifiers. They expect to have prototype Run II preamplifiers by the end of the summer. Coordination with this group is required for the preamplifier design as well as to insure that ICD signals are in time and compatible with calorimeter signals to form the trigger information.

In addition to the change in voltage requirements, the new preamps are also expected to dissipate more heat. Expected power dissipation is 100 mW per low voltage channel, or 300 mW per preamp. [20] We will also have six preamps per drawer, compared to three per ICD box in Run I; so that total thermal power per drawer should be on the order of 2 W.

3.4 Temperature Control and Monitoring

There was no need for cooling of the ICD electronics in Run I. Temperature monitors on the ICD boxes showed no significant heating due to power dissipation form the preamps. However, as mentioned above, the power dissipated by the Run II preamps is expected to be a factor of 10 greater. Due to the closed drawer system, which restricts the flow of air around the ICD electronics, and the higher power dissipation of the Run II calorimeter preamplifiers, we expect temperature monitoring and control may be a more important issue with the Run II ICD. We are currently testing the need for a dedicated cooling system, using Run I preamplifiers and mother boards mounted inside prototype drawers. This will give us an indication of the amount of heating to expect (with the additional power of the new preamplifiers taken into account) as well as providing a model for optimizing the number and placement of temperature probes.

Should cooling be necessary, we plan to try the following solutions :

- Add a heat sink below the motherboard in thermal contact with the aluminum side of the drawer. This will allow heat to be dumped outside of the drawer. We envision that this step should be sufficient. If not, then
- We can add fans to force air between the ICD drawers.

3.5 PMT Testing

Most or all of the PMT's to be used in the Run II ICD will be salvaged from the Run I ICD boxes. These boxes were decommissioned (removed from the DØ detector) and shipped to UTA in the last half of 1996. Before removing the PMT's from the Run I boxes, the boxes will be placed in a cosmic ray test stand similar to that used in Run 1 for two reasons:

1. These PMT's were all operational at the end of Run I, but some time has passed as well as these boxes have undergone movement during decommissioning and shipping. This initial test will show any catastrophic failure of these PMT's due to time or mishandling during decommissioning.

2. A baseline calibration can be obtained on a tube by tube basis to compare to future tests as well as past Run I calibration.

After this initial testing, the PMT's will be removed from the Run I boxes and tested in an LED-based PMT test stand. This PMT tester has been built and is operating at UTA. A description is included in Appendix D and further details can be found in Reference [21]. It provides a high data rate, linear testing of PMTs.

All the ICD PMTs will be retested before installation in the new PMT crates electronics. Testing includes a determination of optimal operating voltage for each tube. Two or more tubes will be operated under the same high voltage supply, PMT's will be grouped by operating voltages to minimize use of trim resistors to facilitate voltage matching between tubes sharing the same supply.

3.6 Number of PMTs per HV

In the run I ICD detector each ICD 'box' contained three PMTs supplied by a single high voltage supply. Because the upgraded detector contains one-half the number of channels compared to the run I configuration, this makes it possible to reduce the numer of PMTs per HV supply from three to two. In this section we describe the arguments for this new arrangment.

The run I ICD consisted of 256 boxes, 128 per cryostat. With three PMTs in each box, we were thus allotted 256 HV supllies. The upgrade design calls for one-half the total number of channels, or 384. We could therefore run two PMTs from a single supply, requiring a total of 192. Based on our experience with the run I detector there are two significant factors which motivate this option.

During run I only a relatively small number of ICD photomultiplier tubes failed. However, in almost every case, a single PMT failure forced us to shut off the HV to the box, due to noise ("sparking") from the defective PMT propagating to the remaining two good tubes in the box. The result was that the failure of one PMT generally meant the loss of three ICD channels. This situation would certainly benefit from reducing the ratio of PMTs per HV supply, particularly in light of the age of the PMTs (approaching ten years by the start of run II), and therefore the increased probability of failures.

One of the goals in calibrating each ICD box on the cosmic ray test stand was to achieve uniformity in response from channel-to-channel. This was done by a combination of tube matching during box assembly and high voltage/trim resistor settings based on cosmic test results. Despite every effort to match the channels as closely as possible, there were still significant variations, owing mostly to the availability of a single HV supply for the three PMTs in a box. Figure 3.6 shows a distribution of ICD channel response (measured in ADC counts/MIP) for a sample tested during run I.
As indicated in the plot, gain variations greater than a factor of two were unavoidable, despite tube matching and tuning trim resistors on the base cards. Such variations raise concerns about the dynamic range of the PMTs.

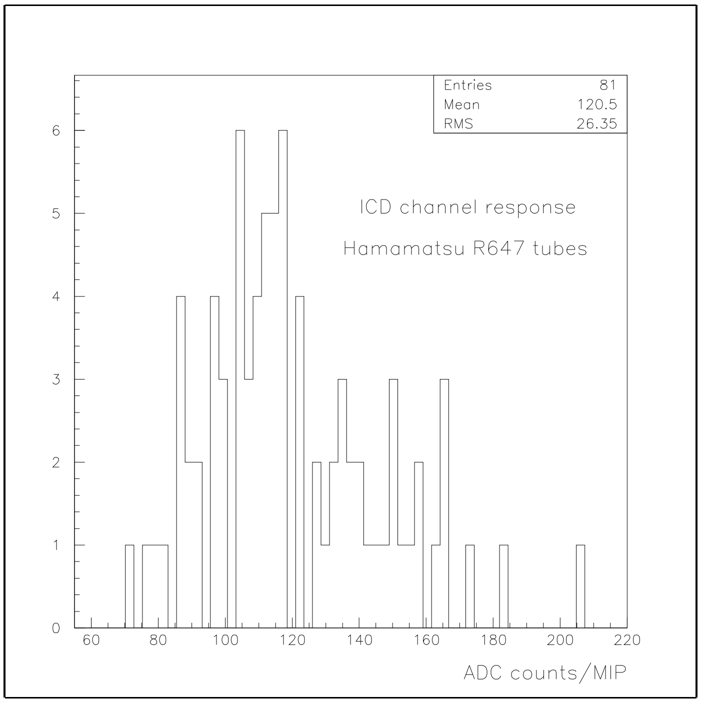

Figure 3.6: ICD MIP response for a sample of R647 channels.

3.7 Mechanical Support

The iron block, necessary to shield the PMTs from the magnetic field, adds a significant amount of weight to the ICD crate. The weight of the iron block is approximately 275 lbs, and the other crate contents bring the total weight to 425 lbs. In addition to supporting the crate's weight, the iron will be subjected to additional magnetic forces in the vertical as well as horizontal directions as described in Chapter 4.

The final support structure has not been fully designed. It is complicated by the fact that the cable winder directly underneath it is not stationary, making it impossible to bolt any fixed structural member from below the crate. The preliminary plan for support of these crates includes the following features:

- To counter horizontal forces on the iron due to the magnetic field, a support collar will be attached directly to the iron block. This collar will have structural members to attach directly to steel struts welded to the end cryostat. These are the same members which support the pig trough. The motivation behind the collar is to prevent transfer of stresses through the crate itself which might distort it, potentially causing misalignment of the drawers or break the light tight seal of the backplane.

- Vertical support is obtained by attaching a frame with rollers on the underside of the crate. These rollers run along the 2 horizontal rails at the top of the cable winder just below the front and back of the crate (displaced by about 22″ in the x direction). These rails extend fully under the crate in z, and will support the crate over the full range of motion subtended by the cable winder while the cryostats are on the platform.

3.8 Installation

Because partial vertical support is obtained from the horizontal rails of the cable winder, installation of the crate requires that the end cryostats be on the platform. The north crates will be installed first, since the north end cryostat remains on the platform at all times. Its installation will coincide with the north tile module installation followed by cabling installation described in Chapter 5.

The south crate installation must wait for the SEC to return to the platform late in the installation schedule. By this time, the north ICD will be installed and commissioned; with this experience, the south crate installation and commissioning should proceed quickly.

Chapter 4

Magnetic Field Considerations

4.1 Introduction

The PMT configuration used in the Run I ICD cannot be reused in Run II for two reasons:

1. The magnetic field in the ICD box region is well over 1000 gauss, making the Hamamatsu PMT's inoperable regardless of shielding.

2. Space in the ICD box region is much more limited in Run II due to the vast increase in cabling which needs to traverse this region from the new scintillating fiber tracker and other devices inside the central cryostat.

As described in Chapter 2, only the scintillator tile modules will reside on the face of the EC's, with clear fiber cables running the light signal to the PMT's some distance away. As described in Chapter 3, ICD PMT's and their associated electronics will be relocated in crates just below each of the four pig troughs. Field strength in this region is expected to be less than about 300 gauss.

The next section describes the tests performed to determine the nature and amount of shielding required to operate the phototubes without serious degradation to PMT performance. It has been determined that an iron block is necessary to properly shield the PMT's. The sections that follow describe the consequences of the addition of this magnetic material: We find the iron causes a local change in the field and resultant magnetic forces which must be countered in the support structure.

The expected magnitude and angle of the field in the PMT crate region is not well known and has only been simulated. This summer, the solenoid will be installed in the detector. In August or September of 1997, testing of the fields and forces occurs. In order to best understand the technological challenges that may arise due the high field, the ICD group plans to participate in this magnetic field test as described in the the final section of this chapter.

4.2 PMT Shielding Configuration Studies

We have studied the variation of gain in Hamamatsu R647 photomultiplier tubes as a function of magnetic field strength in a variety of both magnetic shielding configurations and magnetic field/tube orientations. We tested four different shielding configurations. Test field strengths exceeded that expected in the DØ Run II environment by up to a factor of three. These studies are reported in detail in Reference [25].

The *axial* angle θ is defined as the angle between the PMT axis and the magnetic field. Every shielding configuration we tested was effective for axial angles of 90°. For some configurations more than others, the gain was found to be highly dependent on the axial angle.

In the detector, PMT tubes will lie in the PMT crates with their axis horizontal running along the $\hat{x}$ axis. Details of the insitu field are shown in the next section. We expect the axial angle of the PMT's with the field to be in the range $40^\circ < \theta < 60^\circ$.

We define effective shielding to be that which allows the PMT gain to be reduced less than 20% at 300 G. We summarize our results for the four separate shielding configurations we have studied as follows:

1. Using an extension of Run I ICD shielding including a combination of μ-metal and transformer steel, PMT gain exhibits a strong axial angle dependence which renders the shielding ineffective for angles less than 85°.

2. A combination of commercial cold rolled steel piping and a μ-metal shield proved highly effective at 90° but was ineffective by 70°.

3. A thick 1020 steel tube (1020 refers to steel of 99.8% iron and 0.2% carbon) plus μ-metal shielding was effective from 90° to about 60°.

4. A rectangular 1020 steel block with a cylindrical hole to accommodate the PMT enclosed by a μ-metal shield maintained effective shielding even with the PMT axis parallel to **B** field lines.

The relative gain of an ICD PMT with this last shielding configuration as a function of magnetic field for a variety of axial angles is presented in Figure 4.1. We also discovered that when the tubes are exposed to magnetic fields they experience a history-dependent change of gain with a relaxation period of many minutes. We conclude that the combination of a 1020 steel block combined with one layer of μ-metal exceeds the requirements of the Run II detector.

Based on these measurements [25], our design includes a single solid 1020 steel block housing all of the PMTs in each readout quadrant. It is possible that we could use steel tubes if they had greater iron purity, say 1010 (99.9% iron), but the cost of iron of greater purity combined with the increased machining cost prohibits this option.

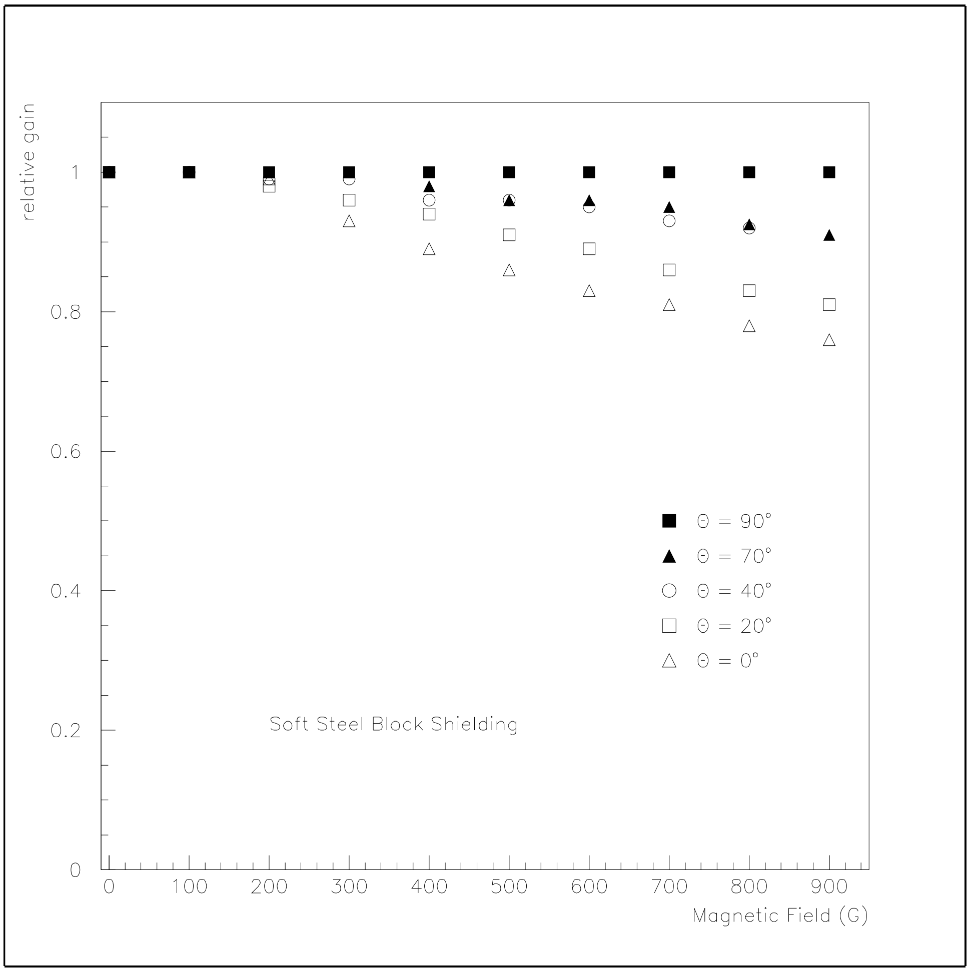

Figure 4.1: The relative PMT gain as a function of magnetic field strength for various axial angles using a rectangular 1020 steel block and a single thick μ-metal shield for shielding.

4.3 Field Distortion and Forces

The magnetic field expected in the Run II DØ detector has been modeled extensively using TOSCA [26, 27], a commercial package which, among other things, can be used to estimate a 3D (static) magnetic field. The use of this program for DØ is described in Reference [28], and references therein. Figure 4.2, taken from Reference [29], is a 2-D

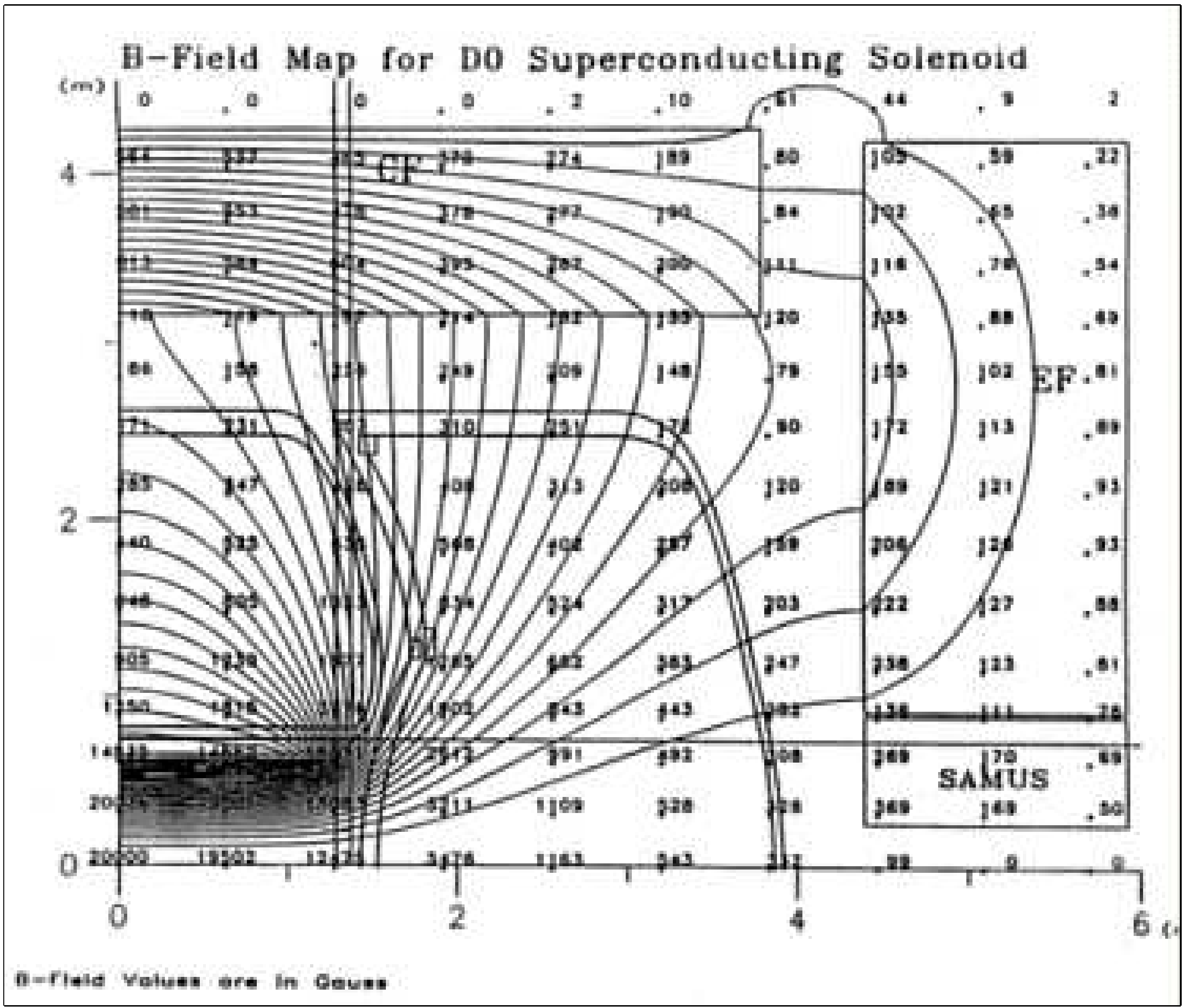

Figure 4.2: Map of the expected magnetic flux with field values superimposed in the Run II detector with solenoid on and toroids off.

map showing the expected magnetic flux lines in a quadrant of the Run II DØ detector.

This particular picture represents the expected field with the solenoid on and the muon toroids off. The $(0,0)$ point coincides with the center of the central detector volume. The outlines indicate the positions of the central and end cryostats as well as the CF, EF and SAMUS muon toroids. Numbers on the figure indicate the expected magnitude of the $\vec{B}$ field in gauss at regular grid points as indicated.

The magnetic field strength on the face of the EC in the region of the ICD scintillating tile array (η of 1.1 to 1.4) is well above 1 kilogauss. The Hamamatsu phototubes could never operate successfully in this environment regardless of shielding. Instead, for Run II, light from the tiles will be transported via clear fiber to the phototubes located in a crate below the pig troughs. In the previous figure, these ICD crates are located just below the end cryostat, where the magnitude of the magnetic field is between 200 and 300 gauss.

Consequences of the introduction of iron shielding for PMTs are a local distortion of the field and additional forces on both the iron and the solenoid itself. In addition, other effects may be important, such as that resulting from quenches, or the routine ramping up and down of the field. These effects are discussed in the following sections.

4.3.1 Magneto-Static Forces

Figure 3.1 shows the top and front view of an ICD crate. The top view features three major subparts:

- The rear section contains the fiber backplane.
- The midsection contains the iron block with holes to enclose and shield the PMT's within it.
- The front contains 16 independently sliding drawers. Six PMT's hang off the backside of each drawer which slide directly into the holes in the iron in the midsection.

The only magnetic material in the crate is the iron block, whose external surface is rectangular in shape. It's faces extend 30.95 inches in $\hat{z}$ and 11 inches in $\hat{y}$. It has 96 cylindrical holes drilled through it's depth (3.5 inches) in the $\hat{x}$ direction. The diameter of each hole is large enough to accommodate one Hamamatsu 1/2 inches diameter phototube inside a μ-metal shield. The true weight of a single iron block is about 275 lbs or 125 kg.

The calculations described in this section of the resultant forces due to the addition of the iron for PMT shielding is described in DØ note 3145 [30]. To simplify the calculation, it was assumed that the iron block was rectangular with the same external dimensions but with no holes. This block weighs 156 kg. Magnetic forces on this block due to the field have been calculated relative to the weight of this block.

To be conservative and to reduce calculational complexity, the iron is assumed to be magnetized to saturation in the field. Table 4.3.1, taken from Reference [30], shows

Magnetic Force per unit Weight		
Field Map Calculation	Average F_y	Average F_T
Solenoid + Muon Steel	0.77	0.23
Solenoid + Toroid	0.96	0.39
Solenoid (no steel)	0.64	0.18

Table 4.1: This table shows the magnetic force on an iron shielding block in the vertical ($\hat{y}$) and transverse plane in the 3 field configurations as indicated.

the resultant force per unit block weight on the iron due to the field in the vertical ($\hat{y}$)

and transverse planes. Forces on all four blocks in the $\hat{y}$ direction are positive (upward), countering the force of gravity. The maximum transverse force is 39% of the weight of the block; the block will require support to prevent it from moving horizontally.

Resultant forces on the solenoid are equal and opposite. The calculation assumes that the four iron blocks are distributed symmetrically in both the $\hat{z}$ and $\hat{x}$ directions, resulting in a zero net resultant force in the horizontal plane. The asymmetry in $\hat{y}$ results in a net downward force of 2290 N (234 kgf) While this force is substantial, it is [30]

> "within the design capabilities of the solenoid cold mass support system ... If the working load is revised to include the new force generated by the ICD iron ... this loading remains smaller than the proof-test load of each link and the safety factor on the ultimate decreases slightly (from 8.8) to SF = 7.9 ... It should be noted that the radial and axial forces on the magnet will be monitored as it is charged to full field in the detector so that in any case unanticipated loadings will not jeopardize the safety of the cold mass support system."

4.3.2 Magneto-Dynamic Effects

Time varying fields occur in the normal course of ramping up and down of the magnetic field for polarity changes or other power cycling, or due to quenches. The time scale on which this change can occur can be as fast as about 10 seconds (in the case of a fast discharge or a quench).

Such changes can induce currents in conducting elements which physically intercept flux. The only elements expected to be susceptible to induced currents lie in the ICD crates which house the PMT's and motherboards upon which the ICD PMT bases and preamplifiers reside. Even at the fastest discharge rates, the flux change are not expected to induce large currents because none of the conducting components in the system intercepts significant flux.

All components should be checked for field sensitivity. Particular attention is being paid to the following areas.

- The motherboard layout is not yet finalized, but care will be taken to eliminate the area enclosed by conductors, for example, the HV leads to the PMTs, which could be sensitive to sudden changes of a few volts.
- The ICD system must contain no magnetic components except for the iron shielding blocks.
- Calorimeter low voltage power supplies must be designed for a high field environment. The same types of supplies will be used for the ICD preamplifiers, but these will be located under the platform (well outside the detector), where the field is insignificant in comparison.
- If cooling fans are to be used for cooling in ICD drawers, they must be field insensitive to 400 gauss.

4.3.3 Perturbations to the Field

We assume the perturbation of the field is proportional to the volume over which the iron acts. In relation to the volume of the solenoid and muon iron, the volume of the ICD shielding iron is negligible. Therefore, we expect changes in the field due to this iron to be small and very localized. Objects from collider interactions entering this region of the detector include only muons and jets which punch through the calorimeter. Such jets are by definition ill-measured and muon tracks are not expected to be slowed or deflected significantly by the ICD iron. Therefore we believe the physics impact due to the imposition of this dead material is insignificant.

4.3.4 ICD Operation in the Presence of the Field

The PMTs are oriented in the PMT crate with their long axis running parallel to the detector $\hat{x}$ axis. From the calculations of Reference [30], the average cartesian components of the magnetic field at the location of the shielding block before the iron is introduced ("air-core field") are $(|B_x|, |B_y|, |B_z|) = (91.6, 103.9, 5.2)$. There is very little $\vec{z}$ component to the field. In this position, the expected angle of the field lines in $\hat{y}$ relative to the PMT axis ($\hat{x}$) is approximately 49°. At this angle, only the rectangular block configuration proved adequate as shielding for the PMT's as described earlier in this chapter.

The true angle of the field at each PMT location in the array is unknown. This is because the field in the iron will not be identical in magnitude or direction to the calculated air-core field. Because precise calculations of the magnetization in the iron aren't possible, we propose to directly measure these effects by participating in the solenoid field test, described in the last section of this chapter.

PMT's are not the only ICD component sensitive to field effects. For example, scintillator response is also known to vary in a moderate magnetic field. Therefore, ICD calibration must include an in situ component so that effects of the field are taken into account. These considerations are discussed Chapter 6.

4.4 Participation in the Solenoid Test

An iron block described above will be put in the four ICD crates to shield the Run II ICD PMTs from the magnetic field. This iron will cause a local distortion of the field in this region. Present calculations indicate that

- the transverse force will be less than 39% of the weight of the blocks and
- the vertical force on all blocks is upward, never exceeding the downward gravitational force

in all field configurations (solenoid and/or toroids on and/or off), The corresponding decentering force on the solenoid is non-trivial but within safety limits.

We propose to include these 4 iron blocks in the detector for the D0 solenoid test currently scheduled in the first half of 1998. In addition, one of these blocks could be contained in a light-tight crate which is partially instrumented to

1. measure the field at a few different locations in the crate,
2. measure light using some Hamamatsu PMTS from an LED based or LASER calibration system.

Our reasons for participating in this test are many-fold:

- We have tested the tubes and shielding in a variety of magnetic field environments which we believe reflect the range of possible field configurations. We have found that the tubes are quite susceptible to changes in the direction of the field. While we believe we have found a shielding configuration which will work, local field distortions are difficult to anticipate. We'd like to see how well the phototubes work in the true magnetic field environment.
- We plan to test a prototype electronics motherboard with the modified calorimeter preamps in order to understand the performance of these boards in a "real world" environment.
- We'd like to assure ourselves that the calculation of the field and forces reflect reality for the sake of the safe and reliable operation of both the ICD and the solenoid.
- It will be useful to go through the exercise of mounting the iron in a crate below the pig troughs. In the commissioning of the Run II detector, there will be many other complicating issues. For example, a light-tight rectangular box containing hundreds of delicate fibers (fiber backplane) will be mounted inside the back end of the ICD crate in Run II. We'd rather not do this for the first time during a tight installation schedule a few weeks before we roll in.
- The ICD group is currently entertaining 2 calibration options in Run II. The first is to learn to reuse the Run I laser system in a useful way. The second is to try an LED based calibration system. We will likely test some version of one or both systems in the solenoid test to evaluate its viability.

Chapter 5

Cabling

The are two major cabling issues involved with the ICD upgrade. First, the signals from the ICD tiles must brought to a low magnetic field region where the PMTs will be housed. To accomplish this, we need clear optical cables between the tile modules and the PMT crates. The other issue is the normal cabling of readout signals, high voltage for the PMTs, low voltage for the preamplifiers, and the laser and pulser calibration signals. We may be able to accomplish this task with slight modification to existing cabling.

5.1 Optical Cables

We plan to run a set of clear optical fiber cables from the ICD tile modules mounted on the face of the Endcap Calorimeters (EC) to the PMT crates mounted to the side of the ECs. These cables will consist of a bundle of 1.0 mm clear plastic fibers, potted in connectors and polished, with an outer black dielectric covering. We are considering the following two possibilities for constructing these fiber cables.

- Produce them locally

  The fiber tracking group have developed techniques for producing similar fiber cables, taking the light signals from scintillating fibers to the VLPCs. They have produced 8 m and 11 m cables consisting of bundles of up to 256 fibers [24], wrapped in a commercially-produced covering called "Zipper Tubing". Advantages of this approach include low cost of production, which would utilize normal university resources (*i.e.* students) employed to produce the relatively small number of cables needed. Disadvantages include production startup costs; namely, we would have to build a connector polisher (fairly expensive) and a cable assembly stand. This process is also labor intensive and *extremely* time consuming.

- Have them produced industrially

  We are currently exploring the possibility of having these cables produced in industry. We are awaiting bids from Mitsubishi Optical, who produced some of the cables for the CDF plug upgrade [6]. Advantages of industrial production include high quality of work, and no need to build specialized fixtures. We have the option of furnishing the fibers, have Mistubishi purchase them from Bicron, or use

Mitsubishi's fibers. The disadvantage is that we do not yet know if this is a more expensive option.

In either case, we will use the same connectors for the cables as were used by CDF for the plug upgrade. These are sold by DDK Electronics, and are described in detail in 18. An example is shown in Figure 5.1. Unfortunately the manufacturer only produces ten channel connectors. We will have 24 light signals coming from each tile module, therefore the most straightforward way to use these connectors would be to use six channels per connector, so that we will have four cables per tile module, for a total of 32 cables to each PMT crate, 64 cables per EC, 128 cables all together.

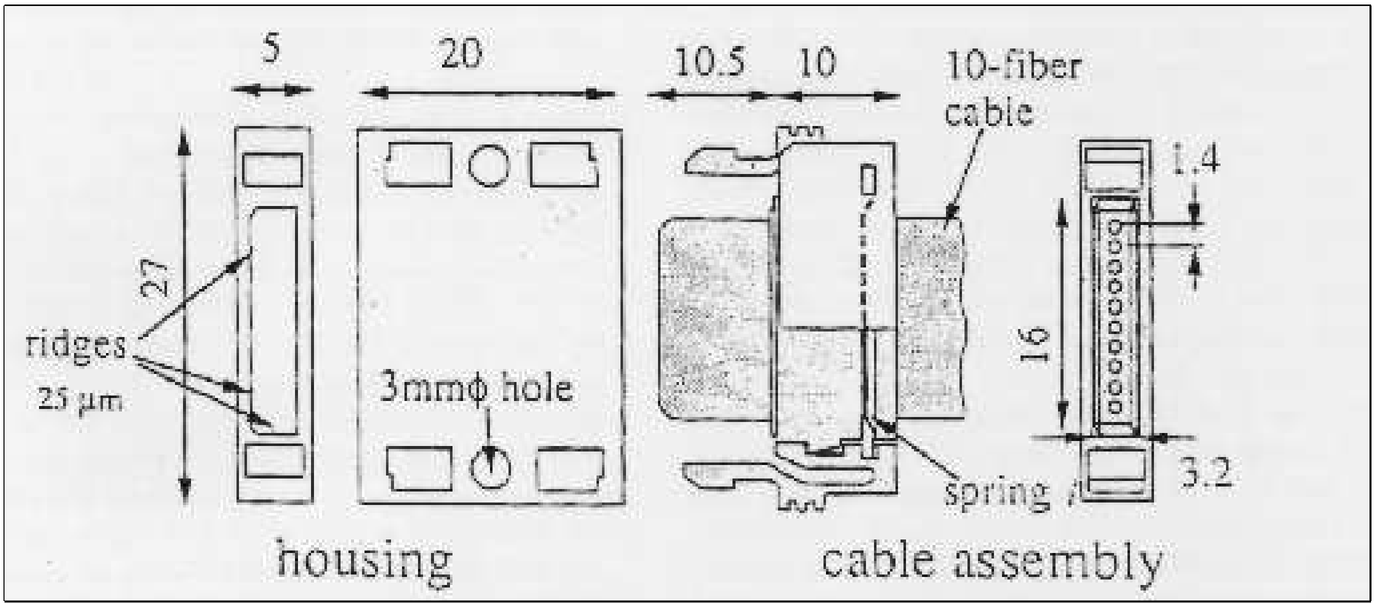

Figure 5.1: The commercially produced connector to be used for the optical cables between the ICD tile modues and the PMT crates.

5.2 Services to the PMT Crates

In the Run I ICD, each ICD box is connected to a high voltage cable, a six line cable carrying low voltage for the preamplifiers and the analog signal cable to the BLS cards, and an optical fiber carrying the laser calibration signal to the ICD tile. (In addition, a sample of ICD boxes also had a temperature monitoring cable.) For the upgrade, there will be a number of changes.

In Run I, high voltage was supplied from power supplies in the movable counting house via eight-line Reynolds cables to high voltage fanouts located on a tray underneath the pig troughs. For the upgrade, these high voltage fanouts (the so-called "Maryland boxes") will be removed. The space formerly occupied by these boxes will provide most of the space needed for the PMT drawers. Therefore we must explore a new way of supplying high voltage to the PMTs. Also three low voltage lines are required by the new preamplifiers. Problems associated with the old six line cables have necessitated that they be discarded.

We propose the following scheme for servies to the PMT drawers :

- One standard HV cable per group of three PMTs be extended from the HV pods to the PMT drawers, and then fanned out internnaly on the mother board to the individual PMTs. This is the same ratio of HV channels to PMTs as in Run I, and will necessitate two HV cables per drawer.
- One calorimeter low voltage power supply be used for the four ICD PMT crates. This low voltage supply will be connected to a local four- way fanout, which in turn will be connected by multiline cables to a new fanout card below each PMT crate. This fanout system will filter the three low voltages (+8 V, -6V, +12 V) and fan them out to each PMT drawer via short LEMO-type coaxial cables (one per voltage).

5.3 Signal Output from the PMT Crates

The signals from the ICD modules were formerly run into 26-line twist & flat cables from the ICD merge cards to the BLS cards. We propose to extend the 26-line cables to the PMT drawers, and remove the ICD merge cards. Only about half the signal line will be used due to the removal of the outer boxes; however we will have to preserve the current mapping of channels, which goes into the formation of trigger towers.

5.4 Pulser Calibration Signal

For Run I, the ICD had it's own pulser. The pulser signal ran into the ICD merge cards and was then fanned out to the ICD boxes. Each merge card carried one pulser signal per ICD box, or one pulser signal per three channels. With the removal of the merge cards, we will have to find a new method for distributing the pulser signal to the ICD drawers. One option is to run a cable from the ICD pulser to the PMT crates, where the custom fanout card mounted below the crate will fanout the signal to the drawers via a short coaxial jumper.

5.5 Optical Calibration Signal

With the LASER calibration option, we will reuse the four fiber trunklines to carry the LASER signal to the PMTs. These trunklines which will run from the LASER housing in the Movable Counting House to the each ICD fiber backplane. For the LED calibration option, power and control lines for the LEDs will have to be run to the fiber backplane. As this system is still being developed, final cabling requiements are not yet known. See chapter 6 for more details.

With the preferred options listed previously, there would be :

- Two standard high voltage cables per drawer (32 per crate).

- One signal cable per drawer (16 per crate).
- One low voltage multiline cable per crate.
- One pulser cable per crate.
- Four short jumpers (low voltage plus pulser) from the fanout card to each drawer.

This layout is shown schematically in Figure 5.2.

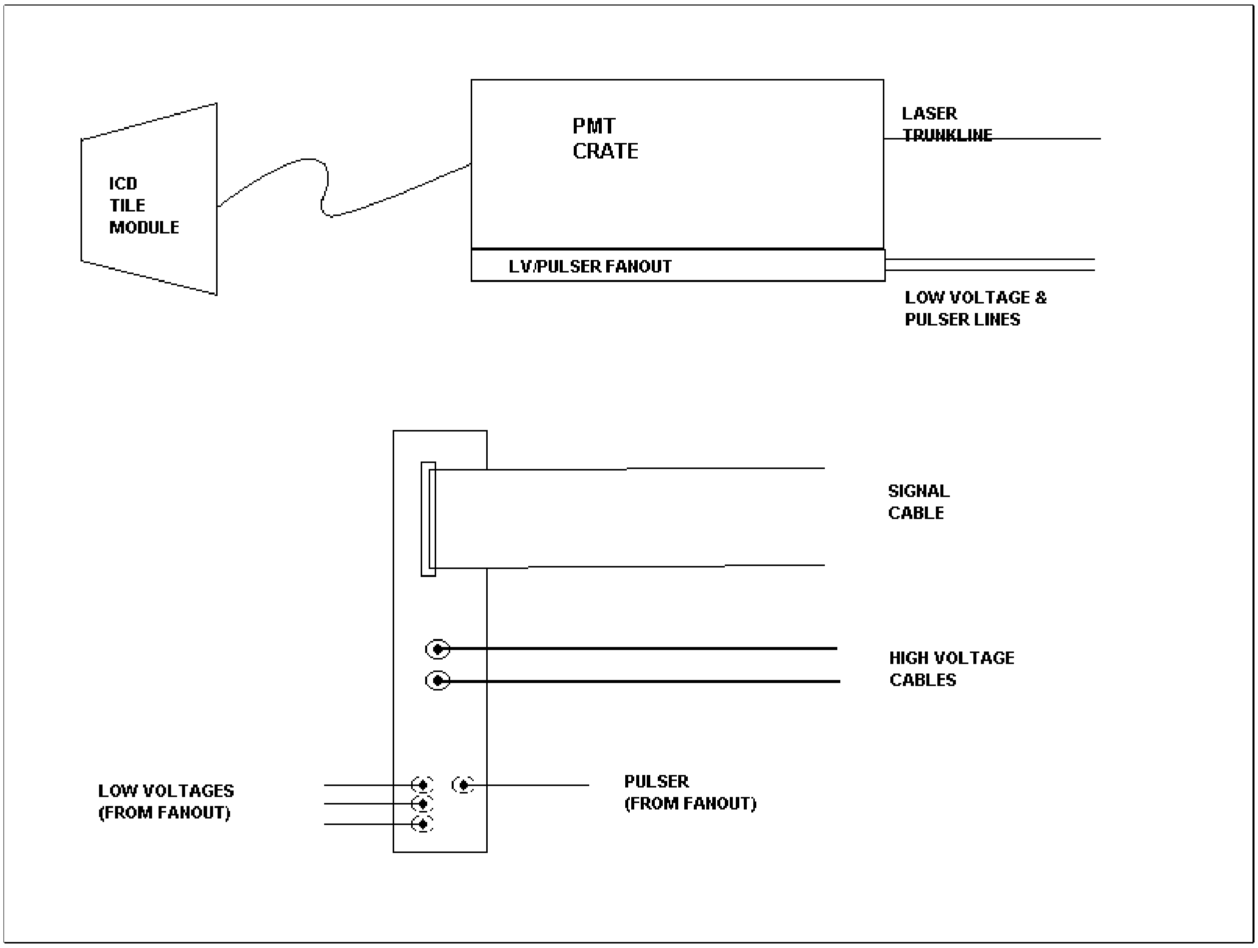

Figure 5.2: Proposed layout of ICD cabling, assuming both low voltage and the pulser signal are fanned out locally at the ICD PMT crate.

Chapter 6

Calibration

6.1 Strategy

The ICD in Run I was intended to be calibrated primarily with a laser source and an optical distribution system that monitored the time-dependent behavior of each channel in the detector. A schematic is shown in Figure 6.1. The initial tile-to-tile variation was tracked with cosmic ray testing, and further channel-to-channel corrections could be made using collider data and symmetry. The phototube amplifiers are standard to DØcalorimetry and are calibrated with the usual charge pulser.

The calibration of the upgraded ICD is different for two reasons. First, the input signal is applied at the phototube, rather than at the scintillating tile. The tile-to-tile and fiber-to-fiber variations must therefore be accounted for by pretesting and symmetry checks *in situ* . Incidentally, since the light will now be delivered directly to the PMTs, less light has to be generated at the source. Secondly, the phototubes are now in a much more accessible spot, making delivery of the light to the phototubes a more straightforward matter, and in fact allowing for more technological options. There will also not be a Level 0 trigger system requiring light flashing in Run II. Otherwise, the system requirements for monitoring channel-to-channel time-dependent variations are essentially unchanged from Run I.

The need for a new system is dictated by the performance of the laser-based system used for Run I. Despite a considerable R & D effort with this system, there was a 3% variation quadrant-to-quadrant in Run I. While the source of this variation is not completely understood, there is clear evidence that the dominant culprit is the migration of the illumination pattern over trunk lines and optical fan-outs closer to the tiles.

In situ calibration with collider data is also demanded by the presence of the magnetic field. General studies [22] have exhibited an $\sim 0.8\%$ per kgauss change in scintillator output due to an external magnetic field. This shift will be undetected by a calibration that excites the PMTs. A calibration system with a moving source is impractical because of the limited space available. Charged tracks in the detector with and without the magnetic field will be used to correct for the performance shift of the scintillator.

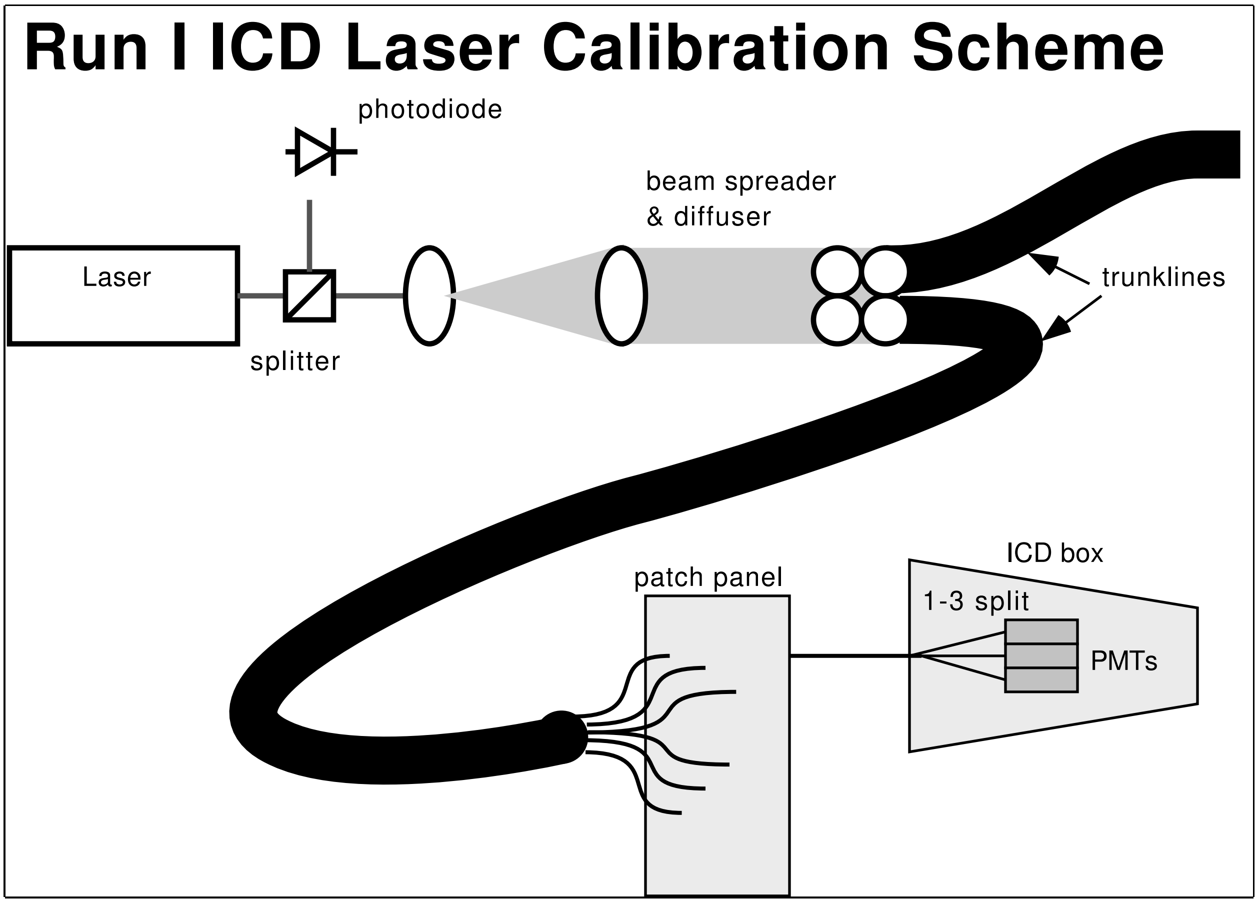

Figure 6.1: Laser system used to calibrate Run I ICD.

6.2 Laser versus LED

Two options for hardware calibration are being pursued. Selection will be based on performance of prototype systems and cost.

6.2.1 Laser

One solution is a modified version of the existing laser system that is designed to avoid some of the problems associated with the migration of the illumination pattern on the trunk lines. Previously, the homogenization of the light was assumed to happen at the laser-end of the trunk lines and at the 1-3 split at the ICD boxes. Instead, we would now treat each of the four trunk lines as a single (multiconductor) pipe that delivers the light to a distribution can that fans the light out to the 96 channels needed per half-end.

The distribution can is a disk of scintillator in the PMT crate (and therefore very close to the PMTs) with 108 WLS fibers (96 signal and 12 for spares and monitoring) on the perimeter. The scintillator receives all the light from the trunk line and homogenizes it, thus eliminating the impact of fiber-to-fiber variation inside the trunkline that contributed to the time-dependent variations seen in Run I. There is no further splitting of the light before the PMT. There remains a fiber-to-fiber variation from the distribution can, which is related to the optical coupling between the scintillating disk and the WLS fiber, but this should remain stable if secured mechanically and is insensitive to migration of light on the face of the trunkline.

As before, the variation of the total output from the laser is monitored by a PIN diode at the output of the laser (using the beam splitter in the laser optics). Migration of the beam spot over the bundle of four trunklines will still result in a trunkline-to-trunkline variation, and this will be monitored by PIN diodes placed at the center of the distribution cans where the trunklines shine on the scintillator. There may be some lingering azimuthal asymmetry at the perimeter of the distribution disk from illumination variations within the trunkline, despite the homogenization of the light by the scintillator. Prototype tests will use four of the twelve spare fibers in the distribution can, monitored with more diodes, to check this possible source of error. If there is evidence of significant variation, they will be left instrumented this way in the final detector.

The schematic of such a design is shown in Figure 6.2. The advantages of such a system are:

- Most of the hardware, especially the expensive laser and trunkline components, already exist.
- The safety issues with the laser have been solved.
- The light source is common to all channels and therefore can be monitored in a straightforward way.
- There is only one channel of electronics required to drive the laser.
- The light pulse shape is clean and fast.

The disadvantages of this system are:

- The instability of the Run I laser system is still not completely understood, and the new design may not address all the problems.
- There is still substantial optical fiber required.
- The required shifting of the wavelength to the green at the distribution can is an inefficient process, reducing the light that actually arrives at the PMT. This is not a likely show-stopper.

6.2.2 LED

An alternate approach is to use LEDs to illuminate the PMTs, a system completely different from the previous laser system. An LED system is currently being developed for the muon scintillator walls, and so a great deal of technology-sharing can alleviate the R

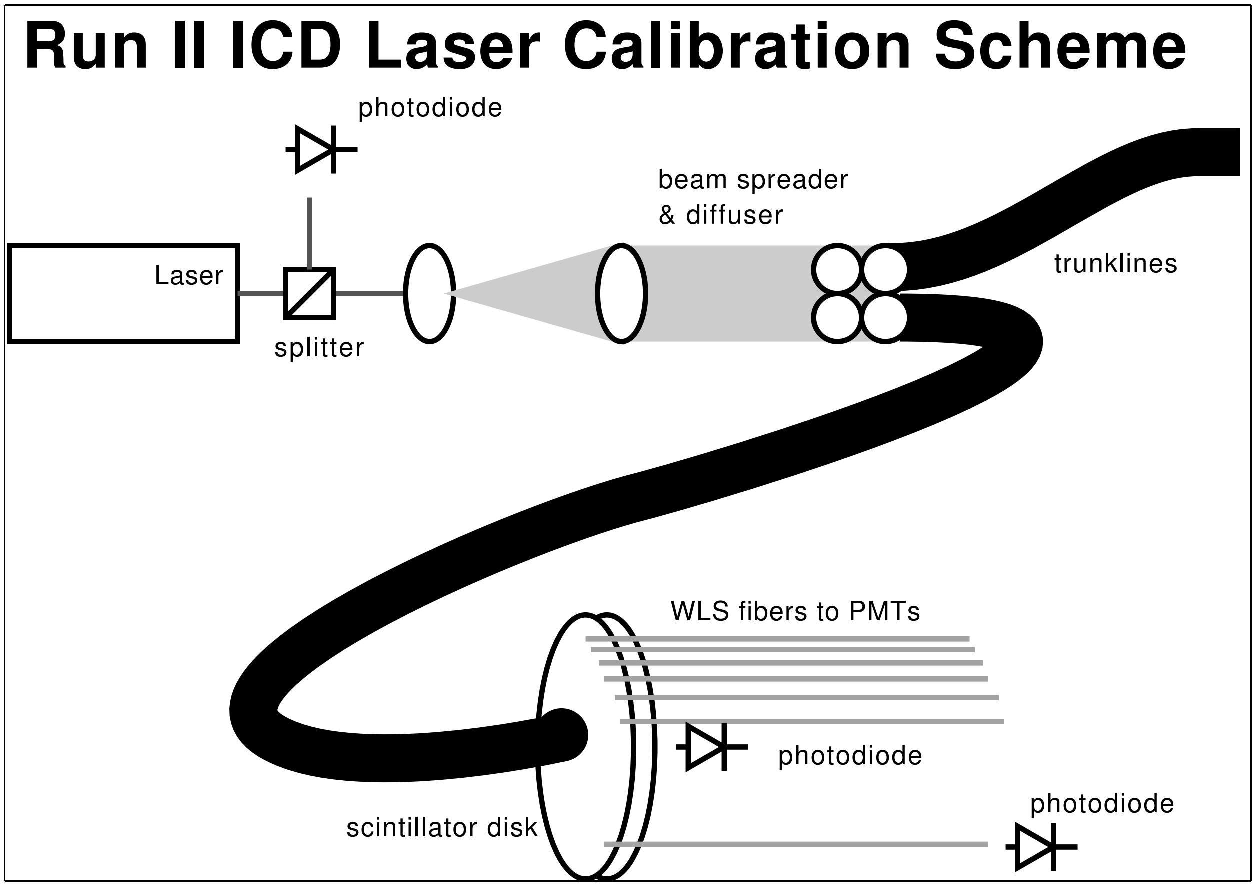

Figure 6.2: In a proposed revision of the calibration laser system, the trunklines deliver light to a scintillator-based distribution can, one in each crate.

& D associated with this new system. LED's offer a highly controllable and stable light source, and in this sense they are a natural candidate for the ICD calibration system. The system is simple: a blue or green LED is attached directly to the cookie at the face of the PMT. The LEDs are pulsed by multiplexed pulsers; the muon wall design calls for 12 LEDs per pulser channel. It is likely the ICD would use the same or similar pulser circuit. The timing requirements for the muon system are somewhat more restrictive than required for the ICD, but this does not compromise other performance characteristics.

The LED option is also attractive with the advent of new high-performance gallium nitrate LEDs in the green and blue (450nm) range, manufactured by LEDtronics and Nichia. These LEDs are very bright and fast, and can be driven linearly with a rather conventional pulser circuit without running in a time-clipped avalanche mode.

The advantages of this scheme are:

- No light piped anywhere and therefore no losses or erratic behavior due to optical coupling.

- Mechanical stability is easy.
- The light output from LEDs is relatively stable and controllable.
- There is no safety issue.
- Pulse timing is easy.
- The only cables that go to the crates are for electronic, not optic, signals.
- System R & D is shareable with another group at DØ.

The disadvantages of an LED system are:

- Because there is one channel per PMT, time-dependent variations translate directly into channel-to-channel variations. Furthermore, there is no way to monitor the LEDs except via the PMTs being calibrated. This puts the onus on understanding the stability of the LEDs very well.
- There is R & D associated with a new system.
- The final cost of the new system has yet to be determined.

6.2.3 Prototypes

A single distribution can is being built for the prototype crate to be used in the magnetic field test in the fall of 1997. The trunk line will have to be reterminated.

We have samples of LEDtronics and Nichia LED's and are testing their performance at UTA test stands. We will also be able to instrument the PMTs with a small sample of LEDs and a dedicated pulser in time for the magnetic field tests.

6.3 Calibration with Data

The response of the scintillator to MIPs can be tied to calibration system response using a dedicated cosmic ray stand and MIPs in the detector. The change in response of the scintillator in a magnetic field will have to be tested in a closed detector with tracked particles and jets, though dedicated bench tests can provide additional information. Single particle response will then have to be connected to the response to jets.

One key difference between Run I and Run II will be the lack of detailed test beam information for the latter. For Run I, optimized sampling fractions for the ICR were extracted from the test beam, and these modules were placed in the final detector. Some studies with Run I data confirmed that the calibration constants extracted with 100 GeV pions at the test beam did a good job of leveling the response to jets. However, there could have been more done, such as layer-by-layer optimization of calorimeter resolution in the ICR. Such studies with data will be crucial in Run II. Note that the coverage of the new detector is somewhat different, and the distribution of dead material in front of the calorimeter is also changed, and thus the sampling fractions for the ICD will certainly need retuning.

Single-particle (MIP) response will be tracked with Run II data, using information from the central tracker and calorimeter layers before and after the ICD. (This is the MTC package [23] .) This tracks time-dependent response, with the cosmic-ray test stand data serving as the time-zero benchmark. It also serves as a low-energy connection with jet data. MIPs can be reconstructed in the calorimeter using the same tools used to recognize muons in the calorimeter. The central tracker can be used to select a momentum range that will not contaminate the MIP assumption with relativistic rise effects. MIPs will be the fastest tool for getting relative calibrations tile-to-tile, although at a fixed and low energy.

Jet-jet and jet-photon balancing will be the primary tool for calibrating the response of the ICR to jets. Using azimuthal symmetry between a jet or a photon in a well-understood region of the calorimeter to set the energy scale for the jet in the ICR is a standard approach that was used in Run I. In addition, the sampling fractions in the ICR will have to be reoptimized to minimize the spread due to energy resolution.

Because of the importance of collider data to the calibration of the ICD, it would be useful to start the collider run with special data runs, as part of the program already being planned by the calorimeter group. ICD calibration would require 2-jet triggers and jet-photon triggers, ideally including some heavily prescaled low energy triggers, and with the solenoid both on and off. Tracking information would have to be included for these runs.

Even basic azimuthal symmetry and end-to-end symmetry checks will also help in corroborating information from the dedicated ICD calibration hardware. For the LED solution, where there will likely be several pulser drivers, interleaving of the pulser fanouts among crates will enable pulser-to-pulser normalization using the same symmetry arguments. For the laser solution, azimuthal arguments will check the mechanical stability of the distribution can, as well as providing a handle on variations in illumination trunkline-to-trunkline.

6.4 Commissioning

6.4.1 Software Tools

Various tools and procedures were written and used for commissioning the Run I detector. Examples include ICD specific code in ENDTSK, CALIB and EXAMINE. Similar software will need to be developed to debug the Run II system. Phi symmetry, laser data and pulsers were used to thoroughly check the performance of the ICD during commissioning.

CALIB was a program used to periodically measure pedestal levels and the gains of the calorimeter (including ICD) preamplifiers. This information was stored in a database and downloaded to the frontend processors prior to each data run. During run Ib the ICD laser system was incorporated into CALIB, so that laser runs became part of the routine calibration procedure. Prior to this time laser runs were made at prescribed intervals independent of CALIB.

We prefer that ICD calibration runs (laser or LED) again be incorporated into the equivalent version of CALIB that will be used in run II; this will ensure that all ICD data is available in the same databases reserved for calorimeter information. It is therefore essential that ICD group members take an active role in the development of run II calorimeter software, particularly in those areas requiring algorithms specific to the ICD subsystem.

6.4.2 Timing

The other major upgrade to the calorimeter is the change in electronics necessary to run with the decreased bunch crossing time (396 ns initially, going to 132 ns later in run II). The upgraded calorimeter electronics make use of an SCA (Switched Capacitor Array) readout scheme, which has necessitated both the new preamps and a new BLS system. This system is still under development, and it will be crucial that the ICD readout is properly incorporated in the overall calorimeter DAQ. One important consideration will be the timing of signals. Our current understanding is that the ICD signal must arrive at the BLS within 20 ns of the peak of the calorimeter signal. This is a relatively tight timing budget, and has driven certain design criteria for the ICD upgrade, including the decision to make all optical fibers, fiber segments in the fiber backplane, and signal cables of equal length. Since we are using the same preamps (with the same shaping time) as the calorimeter, signal time coordination should be relatively straightforward, but we recognize the possibility that we may have to add delay lines to the ICD signal. This will be addressed during calorimeter/ICD integration discussions over the next year.

Chapter 7

Conclusions

We expect the Intercryostat Detector (ICD) to play an important role in DØ calorimetry in Run II. Just as in Run I, the ICD improves jet energy and missing transverse energy resolution in an otherwise poorly instrumented region of the detector. Considerable changes in the design of this detector were necessary due to the introduction of the central magnetic field. The detector design is based on existing technology. Lasting technical issues should be addressed by prototype tests as well as the solenoid field test.

7.1 Acknowledgments

We thank both Rich Smith and Ryuji Yamada for stimulating and helpful discussions on issues associated with the magnetic field. We are indebted to Rich Smith for performing the calculations necessary to understand the impact of the introduction of the iron block for PMT shielding.

We'd like to thank Russ Rucinski at Fermilab for his ideas on mechanical support of the PMT crates. Thanks to Truman Black at the University of Texas at Arlington for allowing us use of the magnet for the PMT testing,

Appendix A

Splicing Tools

If the length of the WLS fiber from the tile to the module connector proves to be a significant source of light attenuation, the WLS fiber in the tile groove may be spliced to clear fiber as it exits the tile, as described in Chapter 2. The tools for splicing fibers and testing the quality of the splices are described here, assuming this option is taken.

A.1 Splicing Tool

There would be one or two splices in each of the fibers laid in the ICD tiles. The junction is between WLS fiber in the tile groove and clear fiber to the ICD box connector. The method for splicing is heat welding, and we are using a fiber splicer modelled after a similar device developed at Michigan State University [17]. The end product is a fiber welded at the junction between WLS and clear sections, with a plastic sleeve surrounding the junction to provide additional mechanical strength. The choice of material for the sleeve is pending some tests; a clear sleeve will cost some light leakage out of the fiber at the joint, while an opaque white sleeve will prohibit microscopic inspection of the joint.

The issues that are of concern in splicing are primarily those that affect transmission:

- offset in concentricity of the fibers;
- local widening or narrowing of the fiber diameter at the joint;
- axial kinks in the fiber;
- damage to the cladding;
- bubbles or inclusions at the joint;
- incomplete welds that would produce a mechanically weak joint.

After substantial R & D at MSU, transmissions of $95\% \pm 4\%$ were consistently obtained.

The UTA version of the splicer is operationally simple. The two sections of fiber are held by clamp blocks to the left and right of a divided glass ferrule. The inner diameter of the glass ferrule matches the diameter of the fiber plus the plastic sleeve, and is replacable. The top half of the ferrule is mounted to a motor-controlled slide with 2 inches travel, and the bottom half is fixed. The fiber is clamped vertically first. Then the left clamp is moved horizontally to apply horizontal pressure to the junction. With the fibers now butted at the center of the ferrule, a lamp is turned on to apply heat through a collimator to the joint. Once the fibers have been melted and fused, the lamp is turned off and blowers are turned on to cool the joint. Once the joint is cool, the vertical clamps are opened and the fiber removed. The time sequence is controlled by a series of timers to provide consistency from splice to splice.

This device has been designed and built. Its basic operation has been tested, but the tuning for the production of successfully spliced fibers has yet to be performed. See Figure A.1.

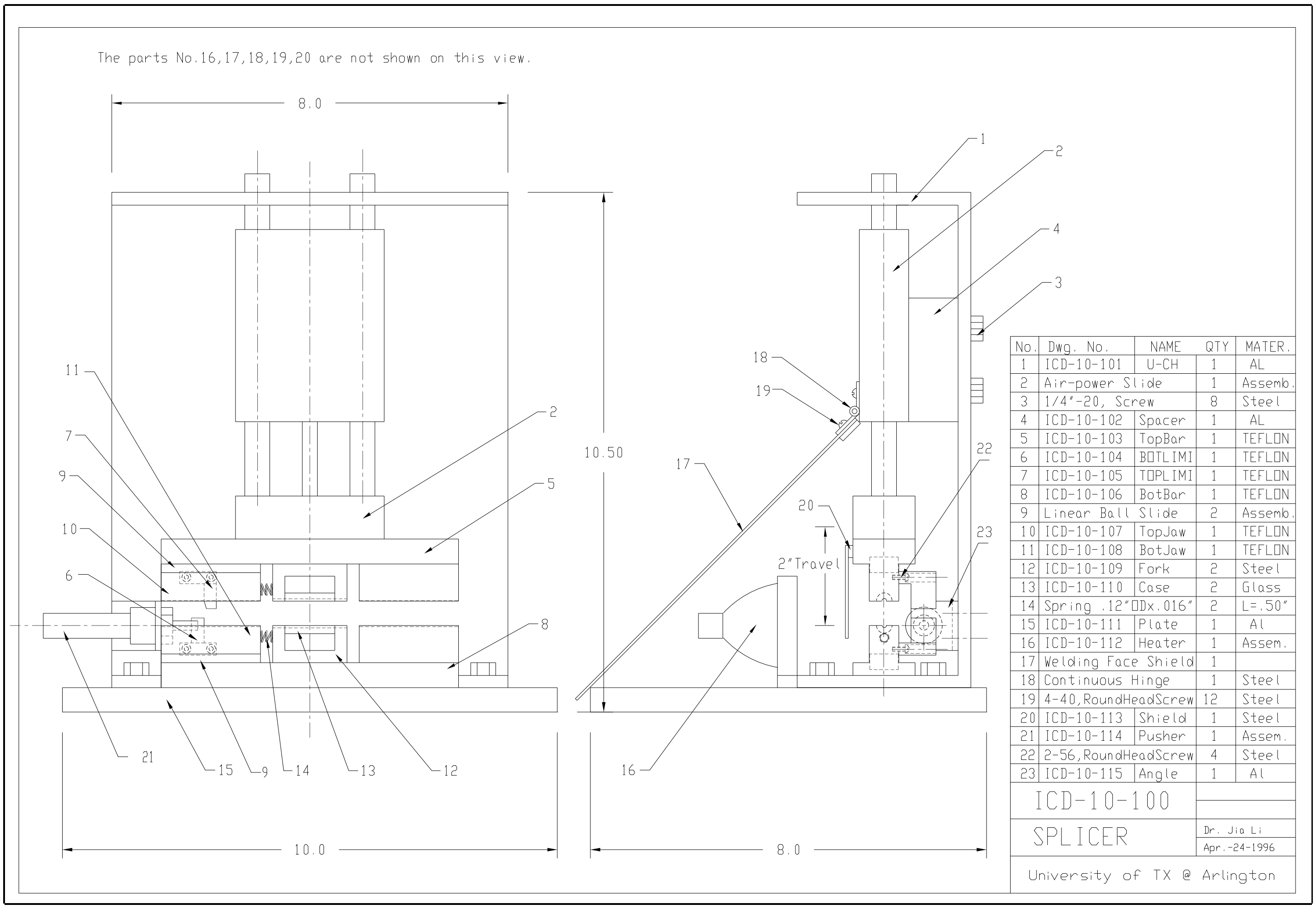

Figure A.1: Assembly schematic of UTA fiber splicer, showing major components.

A.2 Testing the Spliced Fiber

The quality of the splice is, of course, a primary quality control issue. There are two measures of interest: a go/no-go quality check on the transmission of each splice joint based on absolute transmission, and a database of the relative transmission of each of the splice joints.

We have developed and built a splice tester of our own design. The design principle is to simply compare the light output from the ends of a tested fiber with splices with that from a reference fiber without splices. The transmission is simply the ratio of response of the tested fiber to the reference fiber. Because there are different lengths of spliced fibers in the tile box, there will be reference fibers for each length. Light is provided by blue LEDs, whose spectral response is matched to the absorption spectrum of the WLS fiber. Light is monitored by Hamamatsu S1336-18BK silicon photodiodes at the ends of the fiber.

The final configuration of the splice tester depends on the decision whether to read out both ends of a tile fiber (with two splices) or only one end of a tile fiber (with one splice). In the former case, the WLS section of the fiber is between two clear sections, and the two splices should be tested individually. In the end, however, the go/no-go decision will be the logical OR of failures of either of these splices, and the light will be summed by feeding both ends into the same PMT. Therefore we may yet decide to relax this requirement without substantial loss in diagnostic ability. Figure A.2 shows the design with the assumption of this tile fiber. Both reference and test fibers are illuminated in one half of the tester and read out in the other half. The illumination is into the side of the WLS section of the fiber in this case, and is provided by banks of eight blue LED's (four for each fiber) held in the LED block. We have actually allowed for the test and reference fibers to be clamped two different ways. A small clamp block holds and masks a section of the fiber to be adjacent to the LED array. Alternatively, the LED block can be attached to a pair of dummy plastic tiles that will hold the fibers mechanically the same way they would be in the final detector. In both cases, the fibers clamp block is held to the LED block in a mechanically reproducible way with locating pins.

Note that the reference fiber is completely made from WLS fiber, while the test fiber of course has both WLS and clear sections. A correction is made for the differences in attenutation between the clear section of the tested fiber and the corresponding WLS length in the reference fiber. This correction is based on global attenuation length measurements for the fiber spool.

The two pairs of ends of the test and reference fibers are read out by four Hamamatsu photodiodes with low-noise high-gain amplifiers. The response has been shown to be fittable with a second-order polynomial and reproducible, though long-term tests have yet to be conducted. Reverse-biasing the diodes is being considered, though tests so far have indicated that the resultant noise is too large.

If the decision is made to use single-ended fibers in the ICD (with a single splice), illuminating the fiber will be substantially easier, since we will then be able to shine light in the end of the fiber to produce a much higher light yield. The amplifiers on the photodiodes can be then easily modified (with the replacement of a resistor) to a more appropriate gain.

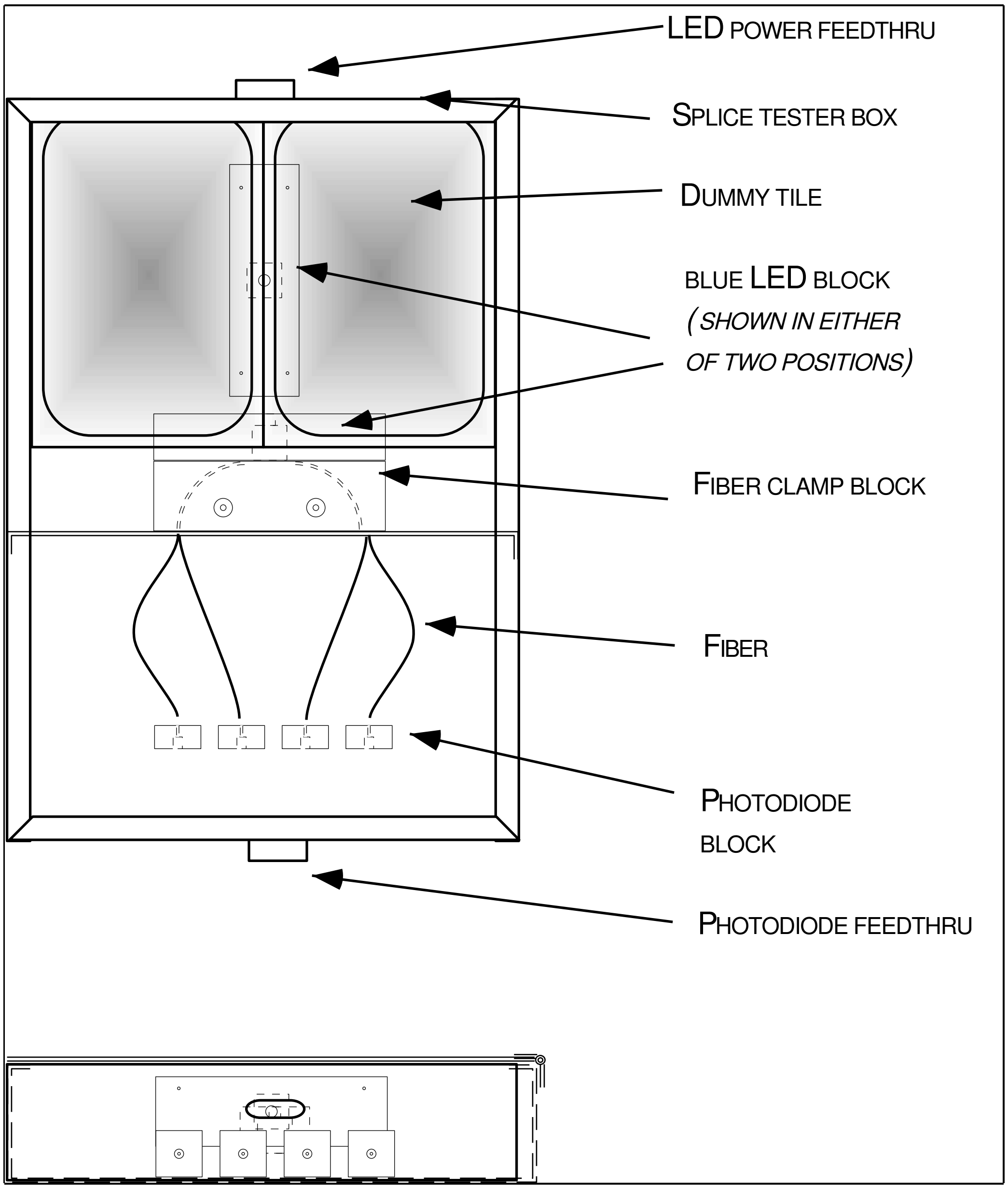

Figure A.2: Assembly schematic of splice tester, showing both standard fiber clamp block and dummy tiles. This version is for the case of fibers read out on both ends, with both splices tested individually.

In this setup, the LED's and photodiodes can be run in DC mode, with the signal from the photodiodes being sampled repeatedly by a standard CAMAC ADC, and the mean response taken.

The operation of the splice tester involves removal of the test fiber while the reference fiber is untouched, and replacement with another test fiber. The mechanical reproducibility of this process, and the stability of the photodiodes are therefore the principle design concerns.

Appendix B

Fiber and Connector Polisher

The polisher designed at UTA is a simple device, modelled after similar devices developed at Fermilab [33]. See Figure B.1. The heart of the device is a flywheel mounted to an AC motor. The flywheel has two pairs of cutting heads, a rough-cut standard machining bit and a fine-cut diamond bit. Both fibers and connectors (that is, single fibers and connectorized fibers) can be polished in this device, the only chief difference being the clamping fixtures that hold the item to be polished.

There are two axes of motion for the cutting action. The y-motion (along the horizontal radius of the flywheel) is controlled by a DC motor, and allows 6 inches of travel. The x-motion (into and away from the flywheel surface) is hand-controlled by a micrometer.

The typical operation will be for the operator to place the fiber or connector in the clamp. A plastic insert in the clamp that holds the item to the flywheel cutter will get polished along with the item to prevent vibration and peeling of fiber cladding, and it is this consideration that will constrain the polishing speed. The micrometer will be set by the operator to move the clamp face to the position of the flywheel face. Then the DC motor will be started and the face of the piece will be moved inward along the radius of the flywheel, first passing by the rough-cut bits and then by the diamond bits. The y-motion controller is then returned to its original position. The operator advances the micrometer and the y-pass repeated.

This device has been designed, and pieces have been ordered and received. It has yet to be assembled and tested. Clamp inserts for the fiber and the connectors have yet to be finalized.

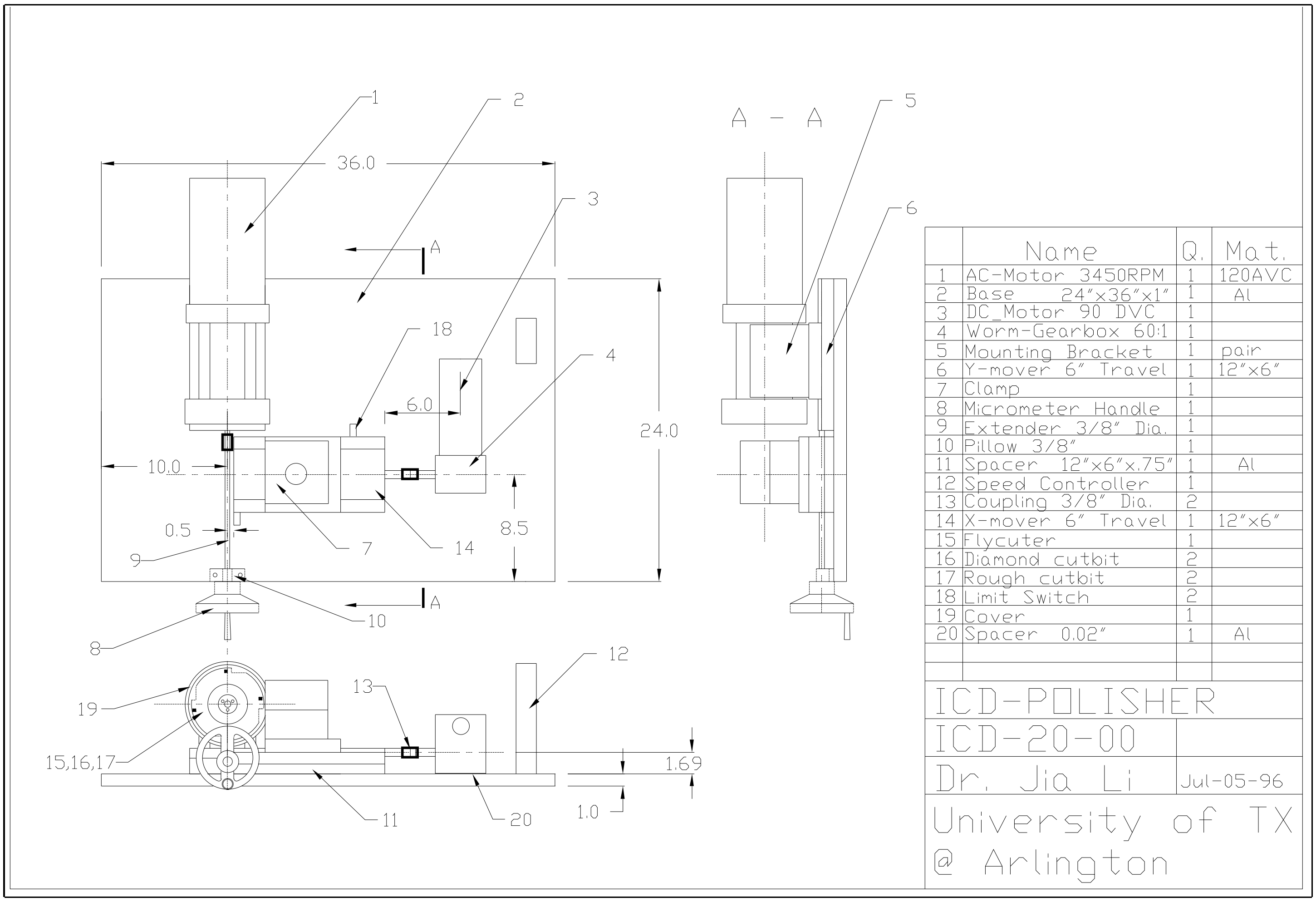

Figure B.1: Assembly schematic of UTA fiber and connector polisher, showing major components.

Appendix C

The Cosmic Ray Test Stands

C.1 Introduction

The Run I ICD cosmic ray test stand was utilized extensively both for tile-to-tile calibration as well as general testing and troubleshooting ICD boxes. Prior to the start of the run, each ICD box was measured on the test stand to establish the initial calibration. Over the course of the run, all ICD boxes were removed from the cryostats (in many cases several times) for recalibration. This information, combined with data from the laser system, was crucial for monitoring and correcting for variations in PMT gains.

Based on this experience, we have constructed a new version of the test stand for the Run II detector. The desired functionality of the new test stand is the same as that of the original one:

- provide a relative tile-to-tile calibration,
- measure tile uniformity and efficiency, and
- establish the level of cross-talk between channels.

But the Run II design is necessarily very different from that in Run I in order to accommodate the Run II ICD scintillator tile modules and fibers.

C.2 Design of the Test Stand

The most significant redesign incorporated into the Run II ICD test stand is the handling of ICD tile modules and fibers. For Run I, ICD boxes were self-contained modules, in the sense that each box housed the scintillator tiles along with the photomultiplier tubes and associated electronics. In the Run II ICD, tile modules will be attached to the EC cryostat walls, but the PMTs and electronics will be situated remotely in drawers a considerable distance from the tiles. As shown in Figure C.1, the new test stand includes a light-tight enclosure for housing an individual module while it is being tested.

In addition to the tile module, the light-tight box also contains the PMTs. They are mounted in groups of three on the inside walls of the box. Adjacent to each set of PMTs are circuit boards with the bases for the tubes. Both ends of each fiber loop (one per channel) are mated to the face of a PMT. The same set of (12) PMTs and fibers will be used for all testing, except in the event where a failure necessitates their replacement. Connections for HV inputs and output signals from the PMTs are routed to patch panels in the front and sides of the box. Each time a new tile module is prepared for testing, the fibers are inserted into the grooves in the tiles by hand and the tile module placed into the box.

C.2.1 Triggering

The test module is placed inside the light tight box at the center of the test stand. Seven scintillator paddle-PMT combinations serve as trigger counters. Three trigger counters are located on the platform approximately three feet above the test module. The remaining 4 counters are on the platform three feet below with their long axes perpendicular to the 3 counters on top. The regions of overlap between the sets of counters correspond to the 12 individual channels on a tile module. A top view of the overlap of trigger counters with the test module is shown in Figure C.2.

C.2.2 DAQ and Test Procedure

A trigger is formed by the coincidence of hit patterns in the top and bottom counters. We are currently evaluating the rate of "good" compared to spurious hits in the counters to determine the necessary level of complexity in the trigger logic. The signals from the PMTs are digitized with an ADC. Once the trigger signifies the passage of a cosmic ray muon through one of the channels in the tile module, the digitized signal is stored on a PC for analysis offline. It is necessary to collect a sufficient number of events such that the Landau peak is clearly discernible—this ensures that the distribution can be fitted with minimal uncertainty. A database of these constants will eventually be incorporated into the overall ICD calibration scheme.

C.3 Conclusion

We have designed and constructed a new version of the cosmic ray test stand that proved extremely useful for the Run I ICD. The new test stand uses an array of trigger counters to signal the passage of cosmic ray muons, in analogy with the previous setup. However, the arrangement of scintillator tile modules and remote PMTs connected by fibers in the Run II ICD made necessary the design of a new light tight enclosure for housing tiles while they are being tested. This new test stand is nearing completion, and will be ready for operation sometime in April (1997).

This new test stand will first measure the light yield of prototype tiles to determine the optimal scintillator tile thickness. Prototypes of thickness 5 mm and $1/2''$ are currently in preparation. Beyond this, the test stand will allow us to quantitatively identify sources of light loss. The final design, combining tiles, connectors, fibers and PMTs, will reliably produce an unambiguous ICD signals with a calibration capable of distinguishing a MIP as well as contribute toward the accurate measurement of jet energies.

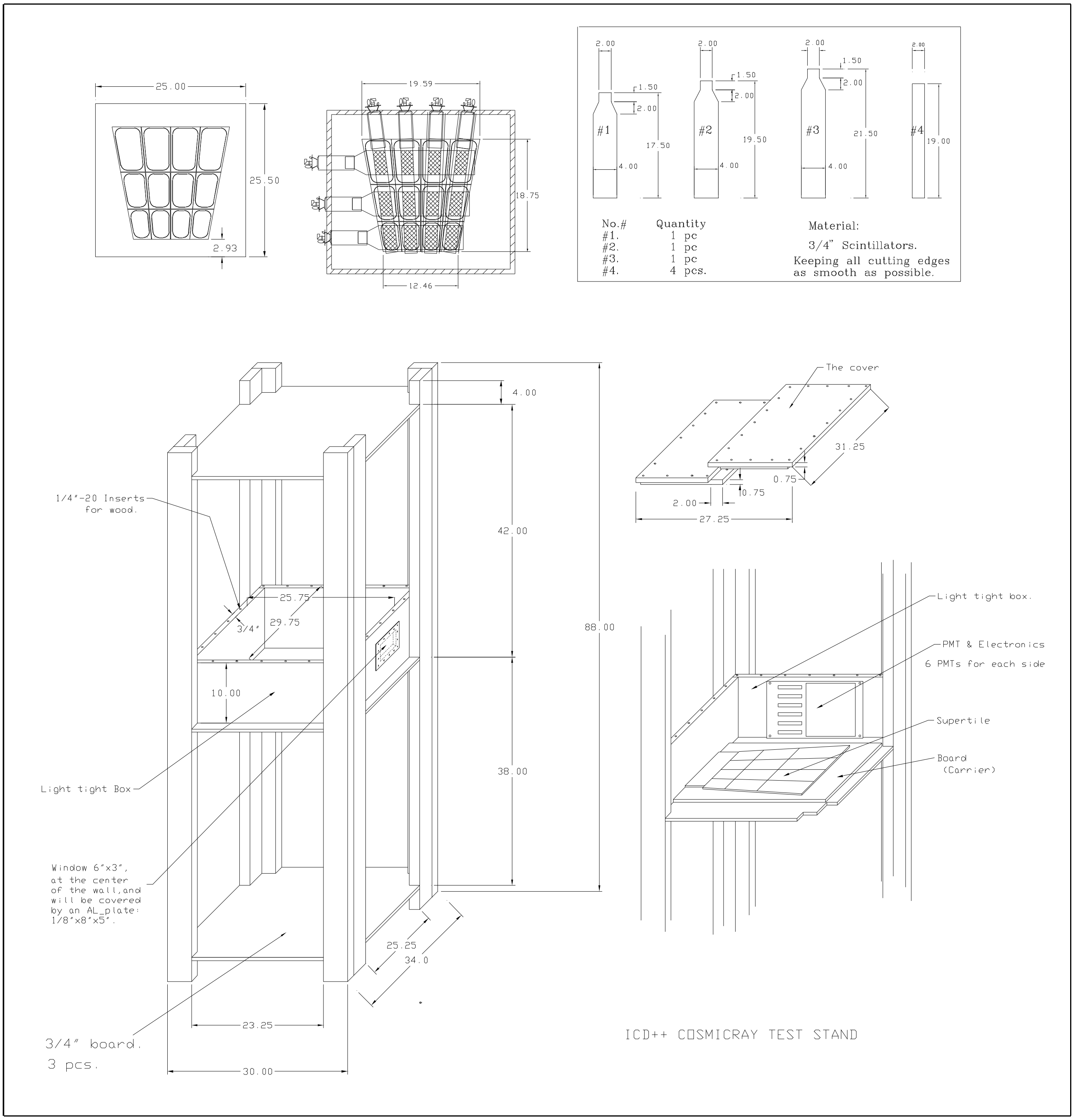

Figure C.1: Cosmic Ray test stand used for testing and commissioning the Run II ICD detector.

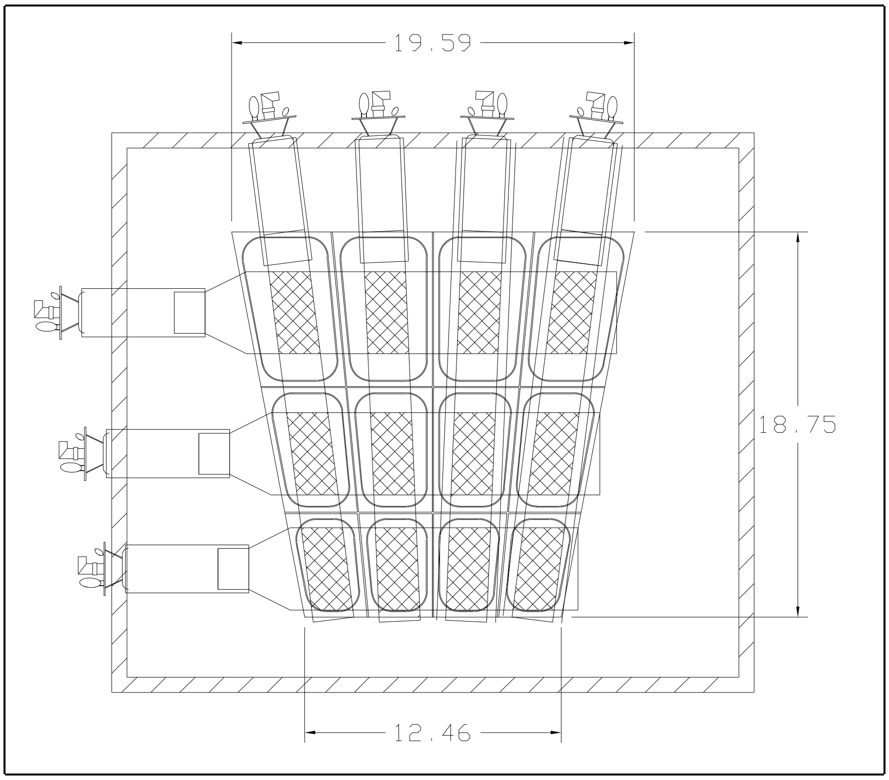

Figure C.2: Arrangement of trigger counters in relation to an ICD tile module.

Appendix D

The PMT Test Stand

The PMT test stand, located at UTA, is fully described in Reference [21]. The photomultiplier tube (PMT) tester simultaneously tests 3 PMTs (inside a light tight box) using a common LED light source. It is run by a Personal Computer.

The computer first determines the range of allowed operating voltages for the PMTs, then gives commands to a timing and sequence module which sets the power levels at which the LED will run. Placed adjacent to the LED is a bundle of optical fibers which lead to the cathode ends of the PMTs. The PMTs are kept in a large light-tight metal box. The output currents from the PMTs are then sent to the preamplifiers that convert the current signals to voltage signals, and then stores them in Sample and Hold (S&H) circuitry. The timing and sequence module commands the S&Hs and tells the ADC when to digitize the data. Later on, the digitized data is sent to the computer for the analysis. This forms one cycle of the testing progress.

Statistical analysis and the characteristics of each PMT are obtained by repeating the above testing cycle many thousands of times at various operating voltages.

The emission of electrons from the cathode of the PMT is governed by the quantum mechanical laws of the photoelectric effect. The number of emitted electrons (n), will thus obey a Poisson distribution with a standard deviation (n = n 1/2). The number of electrons is then multiplied within the tube, and are sent to a preamplifier, which converts the current signal into a voltage. This voltage is converted by an analog to digital converter (ADC) and then sent to the computer.

A flowchart of the PMT test setup is shown in Figure D.1.

Bibliography

[1] D. Schamberger, DØ Internal Note No. 1026, 1990 (unpublished).

[2] T. L. Geld, Ph.D. thesis, University of Michigan, 1993 (unpublished).

[3] M.Sosebee, E.Gallas, K.De; ICD Contribution to the Energy Resolution in the Intermediate Region of the DØ Detector, DØ Note 2519 (1995).

[4] E.Gallas, K.De, M.Sosebee; The Contribution of the ICD to Missing Transverse Energy Resolution in DØś Run1, DØ Note 2494 (1995).

[5] De,Gallas,Li, J.,Sawyer,Sosebee; ICD and EMICD Upgrade Review , DØ note 2402 (12/17/94).

[6] P.DeBarbaro and A.Bodek, editors, "CDF End Plug Upgrade," UR 1389, ER=40685-838, October 1994.

[7] Russ Rucinski (FNAL mechanical engineer), private communication.

[8] Bicron Corp of Newbury, Ohio. Technical Data Sheet for BC400 scintillator, BCF91A WLS fiber (1 mm diameter) and BCF-98 clear fiber (1 mm diameter).

[9] Hamamatsu Corporation, Technical Data Sheet - Hamamatsu R647 series Photomultiplier Tubes (1/2″ diameter).

[10] EFD Corp., 977 Waterman Avenue, East Providence, RI 02914-1378, (401) 434-1680.

[11] Olsson, de Barbaro, Bodek, Budd, Koehn, Pillai, Sakumoto, Walker, Winer "Techniques for Optical Isolation and Construction of Multi-Tile Assemblies in Scintillator Tile-Fiber Calorimeters Using White Epoxy" UR-1370 ER-40685-820, Sept 30, 1994.

[12] Howard Budd (FNAL), private communication.

[13] P. de Barbaro, et.al., "Recent R&D results on Tile/Fiber Calorimetry", UR-1299 ER-40685-748 SDC-93-407, Jan 1993.

[14] Ron Richards (MSU), private communication.

[15] Don Lincoln (DØ CPS upgrade, Michigan), private communication.

[16] P.de Barbaro, A.Bodek, H.Budd, P.Koehn, M.Pillai, W.Sakumoto, J.Freeman, S.Gourlay, "Study of Light Yield and uniformity in Hadron Calorimeters utilizing tile/fiber technology", UR-1354, ER-40685-805.

[17] Benn Tannenbaum, "New Methods in Optical Fiber Preparation for Scintillating Tile Calorimetry", Masters Thesis, Michigan State University (1993).

[18] S. Aota, et alia, "Development of fiber-to-fiber connectors for scintillating tile/fiber calorimeters" NIM **A** 357 (1995) 71-77.

[19] 3M Corporation.

[20] Ashutosh Kotwal, private communication.

[21] Yu Xia "The Characterization of Photomultiplier Tubes using a New Automated Test Facility", Master's Thesis, University of Texas at Arlington, (Aug 1994).

[22] Dan Green "Scintillation Calorimetry", proceedings from SCIFI 93 Workshop on Scintillating Fiber Detectors, Editors A.D.Bross, R.C.Ruchti, M.R.Wayne - World Scientific (Oct 93).

[23] Elizabeth Gallas "Muon Tracking in the Calorimeter", DØ Note 2066.

[24] Manho Chung, SFT group, UIC, private communication.

[25] Ransom Stephens et al, "Study of Magnetic Shielding Configurations for the ICD Photomultiplier Tubes in the DØ Upgrade", DØ Note 2706, (1996).

[26] TOSCA was developed by Rutherford Lab, now marketed by Vector Fields, Ltd., 24 Bankside, Kidlington, Oxford OX5 1JE, England.

[27] J. Simkin and C.W. Trowbridge, "Three-dimensional Nonlinear Electromagnetic Field Computations, using Scalar Potentials", IEEE Proc., 127,6,368-374 (1980).

[28] Ryuji Yamada, Francois Ostiguy and Alex Mesin "2-D and 3-D Display and Plotting of 3-D Magnetic Field Calculation for Upgraded DØ Detector", DØ note 2023, Jan 7, 1994.

[29] J. Brzezniak, et al, "Design Study for a 2 Tesla Superconducting Solenoid for the Fermilab DØ Detector Upgrade", Fermilab-TM-1886, May 13, 1994.

[30] R.P.Smith "Magnetic Forces from the ICD Steel" DØ Note 3145, January 16, 1997.

[31] E. Biagton, E. Goldberg, R. Stephens, J. Harmon, Nucl. Instr. Meth. **B 93**, 296 (1994).

[32] E. Biagton, E. Goldberg, R. Stephens, E. Valeroso, J. Harmon, Nucl. Instr. Meth. **B 108**, 125 (1996).

[33] John Korienek (FNAL), private communication.